The evolution & equilibration of an isolated symmetrically-unstable front

Aaron Wienkers

Supervisor: John R. Taylor

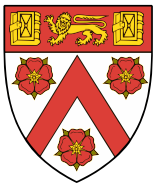

Trinity College

University of Cambridge

January 2020

Contents

Abstract

The submesoscales of the ocean range from 0.1 km to 10 km with time-scales on the order of hours to days. In this range, inertial, rotational, and stratification effects are all important. Submesoscale fronts with large horizontal density gradients are common in the upper ocean. These fronts are associated with enhanced vertical transport and are hotspots for biological activity. Dynamics excited here dictate the exchange rate of important biogeochemical tracers such as heat or CO_2 between the atmosphere and ocean interior. Submesoscale fronts in particular are susceptible to symmetric instability (SI) — a form of stratified inertial instability which can occur when the potential vorticity is of the opposite sign to the Coriolis parameter. The growing SI modes eventually break down through a secondary shear instability, leading to three-dimensional turbulence and vertically mixing the geostrophic momentum. Once out of thermal wind balance, the front undergoes inertial oscillations which can drive further small-scale turbulence, the details of which strongly depend on the ratio of the horizontal buoyancy gradient to the Coriolis frequency.

Here, we consider the idealised problem of a front with uniform horizontal buoyancy gradient in thermal wind balance and bounded by flat no-stress horizontal surfaces. We study the evolution to equilibration of this unstable front using a linear stability analysis and three-dimensional nonlinear numerical simulations. We find drastically different behaviour emerging at late times depending on the relative strength of the front. While weak fronts develop frontlets and excite subinertial oscillations, stronger fronts produce bore-like gravity currents that propagate along the horizontal boundaries. Although the instantaneous turbulent dissipation rate is much larger in strong fronts, the turbulence is intermittent and peaks during periods of destratification. We describe the details of these energy pathways as the front evolves towards the final adjusted state in terms of the dimensionless front strength.

1 Introduction

The upper ocean is a dynamically very active and important laboratory, relevant not only to Earth's climate due to exchanges at the air-sea interface, but to biogeochemical processes throughout the global ecosystem. Length-scales of interest range from planetary scales of $\mathcal{O}(10^7\text{m})$ down to the actively dissipating turbulence scales at $\mathcal{O}(10^{-3}\text{m})$. Dynamics across this range of scales are by no means self-similar, and rather depend greatly on the relative importance of inertial and rotational effects — the ratio of which is termed the Rossby number. This makes constructing a global picture of the ocean energetics an ongoing challenge in the oceanographic community.

The ocean interior and atmosphere communicate through the surface mixed layer. Turbulence acts to vertically-homogenise this upper-most layer of the ocean down to typical depths of 10 to 100 metres. This turbulence may be driven by wind stresses, surface waves, heat or salinity fluxes, or internal flow instabilities. Regardless, the specific properties of the mixed layer determine how permeable this transport buffer is to exchanges of heat, momentum, carbon, oxygen, and other important biogeochemical tracers. Because the ocean interior acts as a reservoir of sequestered heat and carbon, these dynamics within the mixed layer can have an important influence on the Earth's climate system.

1.1 Submesoscales

Dynamics at the submesoscales, in particular, can greatly enhance communication across the mixed layer. The submesoscales in the ocean range from 0.1 km to 10 km with time-scales on the order of hours to days. This range of scales falls between the small, nearly-isotropic microscale of turbulence and the Rossby deformation radius, above which motions become quasi-geostrophically balanced. In non-dimensional terms, both the Rossby and Richardson numbers are order unity so that inertial, rotational, and stratification effects are all important. This means that submesoscale motions are only partially constrained by the effects of rotation and stratification, and so there can be significant geostrophic as well as ageostrophic motions at these scales.

The interaction across scales and between reservoirs of energy enabled by rotation and stratification greatly complicates analysis, at which point theory must be supported by numerics and observation. However, submesoscale phenomena have only recently become a numerically tractable and observationally verifiable domain. Submesoscale dynamics were often too small and fast for both direct ship-borne and remote satellite surveying techniques. Likewise, until the turn of the century numerical models were limited in their dynamic range. These models could only be used for studying either regional mesoscale circulation on grids that were unable to resolve the submesoscales, or focussing on local phenomena with domains too small to represent these structures.

While the mesoscale fluxes can be resolved in regional models, submesoscale fluxes and dissipation often need to be parameterised in global circulation models (GCMs) (Fox-Kemper et al., 2008; D'Asaro et al., 2011; Bachman et al., 2017). These enhanced vertical fluxes by the submesoscales are contrasted to mesoscale eddies which primarily generate *lateral* transport (Capet et al., 2008). Understanding these sources of transport, dissipation, and consequent diapycnal mixing in the ocean is crucial for closing the ocean energy budget and global overturning circulation.

1.2 Cascade Processes

Energy is primarily input into the ocean circulation by air-sea density fluxes and wind stresses, energising the planetary scales, and storing in the large-scale reservoir of potential energy. Fortunately, this reservoir may be tapped by balanced instabilities, converting available potential energy (APE) into geostrophically-balanced kinetic energy (KE). Consequently, 90% of the kinetic energy in the ocean is located in this geostrophically-balanced eddy field, as is schematically demonstrated by the energy spectrum diagram in figure 1. Yet to describe and understand the planetary equilibrium, this energy must somehow reach the dissipative microscales ($\mathcal{O}(1\,\text{cm})$) where viscosity can act. These balanced dynamics of the slow manifold — the mesoscales with scales larger than $\mathcal{O}(10\,\text{km})$ — however, are constrained by stratification and rotation to be nearly horizontal because $Ro \ll 1$. The resulting two-dimensional balanced geostrophic turbulence has inhibited wave-wave interactions and so exhibits an inverse cascade of kinetic energy to large scales (and forward potential enstrophy cascade) (Charney, 1971; Vallis, 2006). Yet *all* of the energy apparently doesn't accumulate at the basin scale…

On its way, this energy can be intercepted and dissipated in part at the surface and bottom boundary layers, as well as by topographical- and boundary-excited waves. Yet there is still dissipation that must

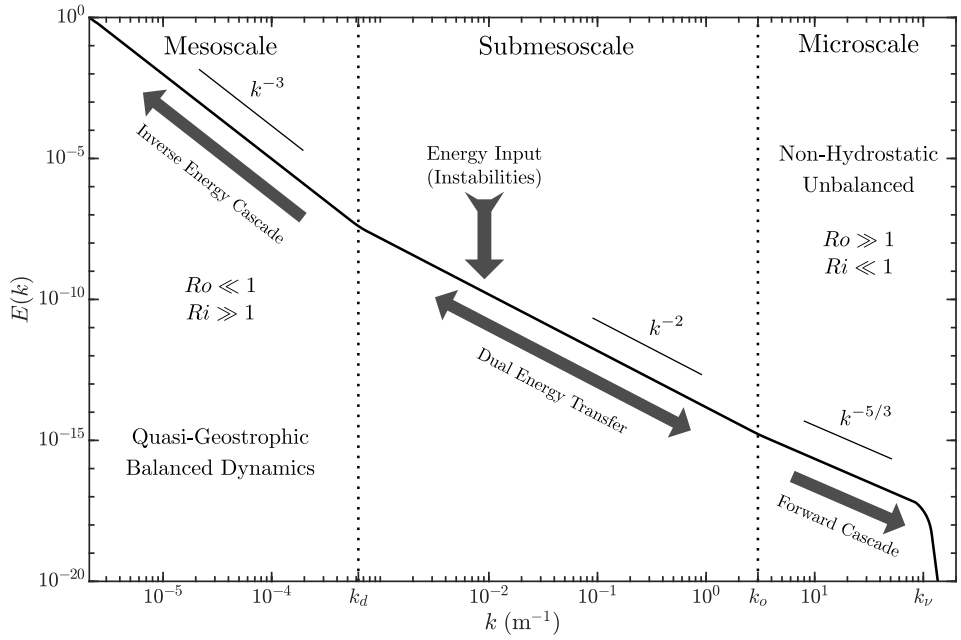

Figure 1: Energy transfers through wavenumber space, showing the classic geophysical and astrophysical fluid dynamics dilemma of the inverse energy cascade at large scales.

be accounted for away from the boundaries, by extracting energy contained in the balanced eddy field via unbalanced dynamics with preferred length-scales into the submesoscale. If this energy reaches scales where rotation is negligible and motions are unbalanced (i.e. $Ro \gg 1$ and $Ri \ll 1$) then the forward turbulent cascade can flux energy onward to higher wavenumbers until dissipated. The processes by which this mesoscale energy can begin a forward cascade has been an ongoing conundrum, and one whose answer lies in the submesoscales (McWilliams et al., 2001). Indeed, unbalanced dynamics support a dual cascade through this bottleneck at the submesoscales (Capet et al., 2008; Molemaker et al., 2010).

1.3 Frontal Regions

Submesoscale structures are commonly found in the weakly-stratified upper ocean. Of these submesoscale features, frontal regions, or local areas with large lateral density gradients and $\mathcal{O}(1)$ Rossby numbers are relatively common. These lateral density gradients in near-geostrophic balance may be set up through frontogenetic strains by mesoscale eddies, or by coastal upwelling, intrusions into intermediate waters, or river discharges.

The presence of a lateral stratification was shown by Thomas et al. (2016) to affect the evolution of the vertical stratification and shear in the frontal region. Fronts with their inherently sloping isopycnals encourage direct exchange between the surface and deep ocean waters due to outcroppings at the surface, further harbouring dynamics which enhance vertical velocities and mixing. The dynamics within fronts (if not the entirety of frontal systems), however, are often unresolved in global and regional numerical models. A better understanding of these self-regulating frontal dynamics is therefore important to modelling the up-scale influence of the submesoscales.

1.4 Plan for the Report

In this report, we consider symmetric instability (SI) as the mechanism for destabilising an initially unstratified front. We review the linear stability analyses, but focus on the energetics of SI and the equilibration varying with the strength of the front. Our three-dimensional nonlinear simulations extend the results of Tandon and Garrett (1994) to allow for turbulent dissipation and to study the late-time frontal dynamics.

While much attention has been given to studying SI independent from the geostrophic adjustment problem, a number of open questions are as yet unanswered relating to SI-induced mixing and the resulting frontal response. Specifically, an initially geostrophically-balanced front is destabilised by way of the vertical mixing of geostrophic momentum during and following the growth of SI. How does the front

then adjust to eventually equilibrate to an SI-stable state, and how does the pathway, final equilibrium, and time-scale change based on the strength of the front?

We take a bottom-up approach to studying the development and equilibration of symmetrically-unstable fronts, focussing on the details of the SI growth and turbulence which quickly mixes the geostrophic momentum and prompts geostrophic adjustment. In section 2, I review relevant literature surrounding submesoscale processes and frontal dynamics. In section 3, we develop the linear stability analysis for a bounded vertical front, and present scalings for the momentum fluxes of these linear modes which themselves may drive ageostrophic secondary circulations. We further consider the stability of the growing SI modes to secondary shear instability, and find a critical mode amplitude beyond which the front transitions to turbulence. We then use these two linear analyses in section 3.3 to determine the efficiency with which the linear SI modes mix geostrophic momentum prior to transition, and discuss the implications for the resulting adjustment process. We present the results of 2D and 3D numerical simulations in section 4.1, specifically looking at the extent to which the mixing of geostrophic momentum induced by SI and turbulence either directly or indirectly prompts a response similar to that of Tandon and Garrett (1994). Finally, in section 4.2 we revisit the numerical simulations to understand the implications of these linear and nonlinear fluxes on the leftover equilibrium inertial oscillations.

2 Literature Review

2.1 Submesoscale Fronts

Previous work on submesoscale fronts is still quite limited. Theory is difficult to advance because many of the submesoscale dynamics are advectively dominated and thus nonlinear. Until recent years, numerical simulations were also largely unable to supplement these problems, as the submesoscales fall in the sub-grid scale of regional models, and yet are too large to be accommodated by the domains of local studies. The dynamic range of the submesoscales was just too broad, and as Brannigan et al. (2017) has shown, under-resolving these scale is detrimental to the accuracy of both the small- and large-scale details.

The simplest model of a front — the Eady model — is a local idealisation of a submesoscale mixed layer front first used by Eady (1949) and later by Stone (1966) and Stone (1970) to study ageostrophic instabilities. The model (shown as a subset of the larger finite front in figure 2) consists of an incompressible flow between two rigid, stress-free horizontal boundaries and which is in thermal wind balance with a linear background buoyancy field, $\bar{b}$, with gradients defined by the squared buoyancy frequency, $N^2 = \partial_z \bar{b}$, and the horizontal analogue, $M^2 = \partial_x \bar{b}$. Because it is a local (and therefore horizontally homogeneous) model, this problem has no natural horizontal length-scale, and so the frontal strength parameter, $\Gamma \equiv M^2/f^2$ (with $f = 2\Omega$ the Coriolis parameter) will be used to parameterise our study rather than the Rossby number.

Due to baroclinic torques, $\nabla\rho \times \nabla p$, which tend to flatten isopycnals, horizontal buoyancy gradients by themselves do not comprise a stable configuration. A balancing torque from the Coriolis force acting on the vertical shear profile, $\partial_z \bar{v}_g = M^2/f$, however, is able to counteract baroclinic torques. This is termed the thermal wind balance, which is a special case of geostrophic balance when the boundaries are aligned with geopotential surfaces such that the horizontal pressure gradients are provided entirely by the background buoyancy gradient.

2.1.1 Observations

A number of observational studies motivate working on frontal regions for their prevalence and relative importance in the upper-ocean energy budget. The main persistent frontal systems in the ocean include western boundary currents (in particular the Kuroshio and Gulf Stream), and the Antarctic Circumpolar Current. Thomas et al. (2013) note typical values of $M^2/f^2 \sim 50$ in the Gulf Stream, and similarly in the Kuroshio. In addition to strong fronts in the core of these currents, mesoscale instabilities can be seen to pinch off rings and mesoscale eddies, which themselves generate sharp transient fronts (Brannigan et al., 2017).

Shallow coastal regions, where the boundaries contribute to vertical mixing and a freshwater outflow provides a strong horizontal stratification, are also sites of strong vertical fronts. Shelf-break fronts and tidal fronts can similarly be maintained by a freshwater source at the coast. Front strengths, $M^2/f^2 \sim 500$, near the northern coast of the Bay of Bengal, and similarly sharp salinity fronts near

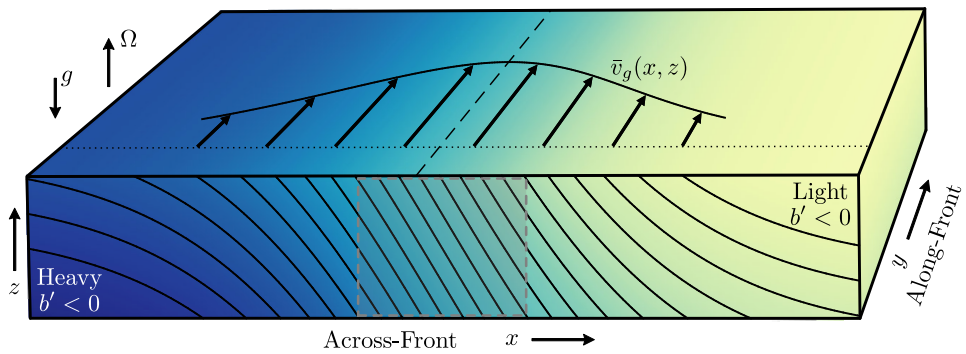

Figure 2: Schematic of a model frontal region showing coloured contours of density varying both across the front and vertically. The across-front stratification is balanced by the thermal wind shear in $\bar{v}_g$, shown on the top face. A local horizontally-homogeneous model can be constructed by considering the region within the grey box, where the buoyancy gradient is approximately uniform.

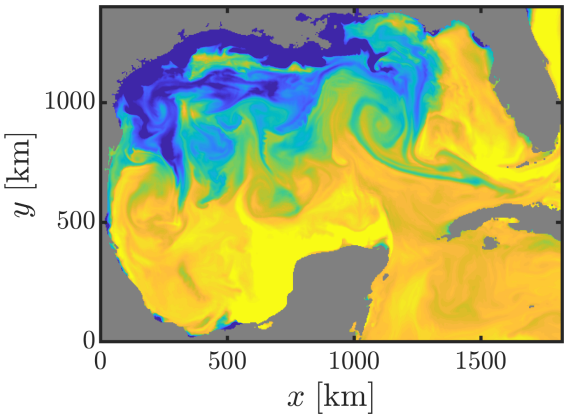

Figure 3: Gulf of Mexico sea-surface density plot on June 8th, 2015 showing strong density gradients generated by the straining field produced by mesoscale eddies. Data generated and provided by the NOAA Regional Navy Coastal Ocean Model (NCOM).

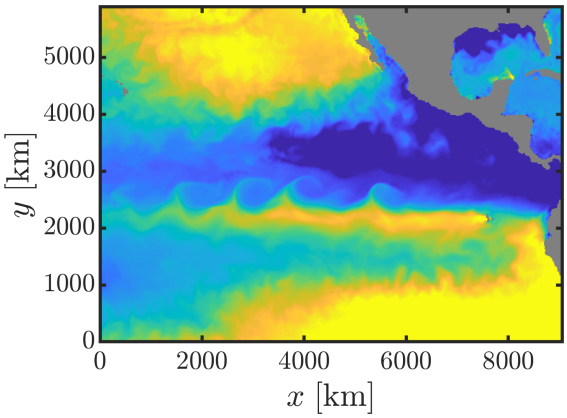

Figure 4: Equatorial Pacific sea-surface density plot showing strong fronts generated by the cusps of a Tropical Instability Wave train on June 20, 2010. The strong La Niña that year generated the cold tongue required to energise the TIW, with a typical period of around 30 days. Data generated and provided by the NOAA Regional Navy Coastal Ocean Model (NCOM).

the Mississippi River outflow in the Gulf of Mexico have been observed, and with a typical surface layer depth of around 10 m (Jinadasa et al., 2016).

Submesoscale fronts and dense, narrow filaments can also be generated by the strains supplied by mesoscale baroclinic and barotropic eddies acting on the weak buoyancy gradients, such as those left in the mixed layer of the Gulf of Mexico and Bay of Bengal (see figure 3). Hoskins and Bretherton (1972) showed that this so-called frontogenesis induced by a background horizontal deformation flow acting on a horizontal buoyancy gradient can generate exponentially increasing gradients. Observations of this process in the Gulf of Mexico suggest fronts ranging from $M^2/f^2 = 1$ to 100 across a typical mean mixed layer depth of 50 m. This frontogenesis in under-resolved and quasi-geostrophic regional models is often arrested by the ad-hoc diffusivity required to regularise and stabilise their numerics near the grid-scale. Indeed, frontal arrest is inevitable, but is rather physically attributed to turbulence and enhanced diffusion due to submesoscale instabilities such as SI (Bachman et al., 2017).

Tropical Instability Waves (TIWs) are a final mesoscale instability known to generate very strong fronts near the equator. First observed by Legeckis (1977), TIWs have a typical period of around 30 days and occur at the interface of equatorial cold tongues. At large amplitude, these waves form cusps as shown in figure 4, which become unstable to a host of submesoscale instabilities, and can eventually generate surface gravity currents as observed by Warner et al. (2018).

Thompson et al. (2016) has compiled glider data surveys in the open ocean, capturing the wide range

of transient fronts which can spontaneously appear. He found frontal strengths ranging from $M^2/f^2 \lesssim 1$ in around 40% of fronts, up towards $M^2/f^2 > 100$ in 1% of occurrences. Many of these transient fronts persist for $\mathcal{O}$(days) and so permit SI to grow and influence their evolution. The exact details of this influence of SI across the wide range of Γ, however, has not yet been systematically examined in the literature.

2.1.2 Potential Vorticity

The Ertel potential vorticity (PV),

$$q \equiv (f\hat{\mathbf{k}} + \nabla \times \mathbf{u}) \cdot \nabla b, \tag{1}$$

is a useful diagnostic in this problem not only because it is a conserved scalar, but also it has some physical relevance to the stability of SI when $fq > 0$. As shown by Haynes and McIntyre (1990), q can only change with time between isopycnals due to the flux of non-conservative terms — the so-called impermeability of PV. PV thus is conserved through purely advective processes, for example, during inertial oscillations of the front.

Splitting the individual PV contributions for a balanced flow, we see that the baroclinicity of the fluid always reduces the PV,

$$q_{bc} = -\frac{1}{f}\left(\nabla_h b\right)^2 < 0, \tag{2}$$

whereas the vertical stratification and vorticity contribution (for inertially-stable flow),

$$q_v = \zeta N^2 > 0, \tag{3}$$

is stabilising (where $\zeta \equiv \omega_z + f$ is the absolute vertical vorticity). Much of the ocean interior is sufficiently stratified such that the contribution (3), overwhelms the baroclinic term to result in an SI stable flow. However, as noted by Thomas et al. (2016), vertical turbulent mixing within the surface and bottom boundary layers results in weakly stratified layers which, in the presence of lateral buoyancy gradients, can generate negative PV. Nearly unstratified (vertical) fronts can even be generated in the wake of mixing events, such as storms, that occur on fast time-scales compared to oceanic times.

Alternatively, one might also note that the baroclinic term (2) could become increasingly negative if f is very small (i.e. near the equator) as pointed out by Hua et al. (1997). However, because in this case $-\omega_z$ could easily exceed f, then this would actually produce an inertial instability.

2.1.3 Parcel Theory for IGWs

To build an intuition for internal inertia-gravity waves in frontal regions, we begin with two important conserved quantities needed to eventually develop the parcel theory for symmetric instability (Haine and Marshall, 1998). Foremost, buoyancy is conserved during adiabatic processes (i.e. without heating or thermosaline mixing), and so parcels can exchange along isopycnals (with slope $s_\rho = M^2/N^2$) with no potential energetic penalty. Similarly, absolute momentum, $m \equiv v + fx$, is conserved for inviscid, unidirectional fronts, as we're focussing on here. Fluid parcels may thus be continuously exchanged along m-surfaces (with slope $s_m \equiv f^2/M^2 = \Gamma^{-1}$) without an inertial response.

We can thus begin by considering internal gravity waves (IGWs) without the horizontal buoyancy gradient of a front. This simply rotating and stratified domain has no background flow, and so the m-surfaces are vertical and the isopycnals horizontal. Now a vertically-displaced parcel across isopycnals will result in a buoyancy anomaly, b', and consequent acceleration, $a = b'$, which sets up vertical oscillations with frequency $\omega = \sqrt{N^2}$. Similarly, to conserve absolute momentum, any lateral displacements across m-surfaces (here in $\hat{\mathbf{x}}$) will gain a velocity anomaly, $v' = -fx$, which then feels an acceleration, $\ddot{X} = fv' = -f^2X$. This similarly sets up lateral oscillations with frequency $\omega = f$. Inertia-gravity waves in this quiescent domain thus exist at frequencies somewhere between purely inertial and purely buoyancy waves, $f < \omega < N$, depending on the phase angle.

Considering the case now of IGWs within a front, the $M^2 \neq 0$ means that isopycnals become steepened, whereas (due to thermal wind balance) the m-surfaces become shallower. While the minimum inertia-gravity wave frequency is still realised along isopycnals, now because the gradient of m along isopycnals is reduced, then the frequency can decrease to (Whitt and Thomas, 2013)

$$\omega_{\min} = f\sqrt{1 + \partial_x v_g/f - \frac{M^4}{N^2 f^2}}, \tag{4}$$

which apparently can go to 0 for small enough N^2. In fact, the temporal growth implied by the imaginary component of ω when N^2 is sufficiently small is exactly SI, showing that SI really is just an unstable subinertial gravity wave.

2.2 Instability in Fronts

The dynamics of these otherwise balanced fronts are often instigated or driven by instabilities of the background state. For example, restratification of the mixed layer is ultimately accomplished by releasing potential energy from the background baroclinic currents, but in some cases may crucially only be accessed by dynamics drawing energy from the kinetic energy of the geostrophic velocity (as is the case for SI).

Instabilities which arise from the mesoscales are the primary mechanisms for producing submesoscale fronts. These balanced quasi-geostrophic instabilities spontaneously emerge from mesoscale eddies, interactions with boundary layers, or topographic wakes, and often take the form of a horizontal inflection-point instability. Examples of such balanced instabilities are barotropic and baroclinic instability, whose dynamics represent a stirring mode. While these balanced instabilities may encourage frontogenesis, they specifically preclude a forward cascade of energy. Once at the submesoscale though, a number of ageostrophic, or unbalanced instabilities can send this energy on its way to dissipation scales (Barkan et al., 2015).

Symmetric Instability is one of several ageostrophic instabilities active in submesoscale frontal regions, including inertial instability, Kelvin-Helmholtz Instability (KHI), and convective (gravitational) instability, all of which represent a loss of balance and so are of interest to this present study (see e.g. Haine and Marshall (1998) for a review).

2.2.1 Kelvin-Helmholtz Instability

Kelvin-Helmholtz Instability is a common shear-driven instability not exclusive to frontal regions, but which commonly arises as a secondary instability in some form (Taylor and Ferrari, 2009). We will indeed see KHI be the mechanism for saturation of the primary SI modes in the present problem. And while it is not dependent on rotation and stratification (in that it draws its energy from the mean kinetic energy), it will be shown in section 3.2.2 that the instability can be modified within a frontal region.

The well-known necessary (but not sufficient) condition given by the Miles-Howard theorem states that there is potential for KHI to grow if $Ri_g < 1/4$. This is not realised in the thermal wind shear of our unstratified front basic state, however, because there is no inflection point to nucleate on.

2.2.2 Baroclinic Instability

The competing instability to SI often is baroclinic instability, which releases the potential energy stored in the horizontal buoyancy gradient, rather than extracting it from the thermal wind shear like SI (Charney, 1947; Stamper and Taylor, 2016). This balanced instability of baroclinic waves has large down-front wavelengths on the order of the Rossby deformation radius, $\mathcal{L}_d/H \sim \Gamma$, with relatively small growth rates on the order of the inertial time-scale whenever the Richardson number is positive (Haine and Marshall, 1998).

Baroclinic instability has received the most attention in previous literature out of all the various submesoscale instabilities. The linear stability was first analysed along with SI in a bounded domain by Stone (1966). Relying on the hydrostatic approximation, he found the linear growth and length-scale for baroclinic instability:

$$\sigma_{\mathrm{BI}}/f = \sqrt{\frac{5/54}{1+Ri}} \tag{5}$$

$$\lambda_{\mathrm{BI}}/H = 2\pi\Gamma\sqrt{2/5\,(1+Ri)}. \tag{6}$$

Thus if the frontal region is of finite extent (narrower than $\mathcal{L}_d$), which is typical of these strong fronts under consideration, then baroclinic instability could be expected to be damped. This question will be an ongoing direction for future investigation.

2.2.3 Gravitational Instability

When the background $\partial_z \bar{b} < 0$, then fluid parcels can continuously rearrange within the gravitational potential and extract energy from the available potential energy stored in the vertical buoyancy gradient.

It's clear then that gravitational instability is just an extension of an internal gravity wave (with gravity a restoring force acting on buoyancy anomalies), but when $N^2 < 0$ so that the dispersion relation $\omega \approx \sqrt{N^2} k_\perp / |\mathbf{k}|$ gives an imaginary frequency.

Here, kinetic energy is generated via the buoyancy flux, $\mathcal{B} = \overline{w'b'}$. Unique to frontal regions is an alternate means of buoyancy production. Specifically, the background stratification can be statically destabilised by a mean cross-front shear advecting the horizontal buoyancy gradient, or similarly by induced surface Ekman flow across the front (Thomas et al., 2013). If this mean motion results in a locally gravitationally-unstable region, then overturning, energy extraction, and mixing may occur.

2.2.4 Symmetric Instability

Compared to gravitational instability, or "upright convection", symmetric instability, termed "slantwise convection" occurs when convective instability is modified by the presence of a front. SI then rather generates slanted overturning circulations which are perpendicular to the geostrophic flow. Contrasting to the potential energy conversion by a full convective instability, SI instead extracts the kinetic energy in the thermal wind to energise the growth.

Specifically, SI is a form of stratified inertial instability which can occur when the Ertel potential vorticity, q, is of the opposite sign to the Coriolis parameter — anticyclonic PV (i.e. $qf < 0$) (Hoskins, 1974). The modes are invariant in the down-front ($\hat{\mathbf{y}}$) direction (Stone, 1966), and is the dominant instability in fronts with $\Gamma \gtrsim 1$, having growth rates on the time-scale of the lateral stratification, $\sqrt{M^2}$.

Much attention has been given to the stability and behaviour of the Eady model since his original analysis in the atmosphere (Eady, 1949), extending the unbounded analysis by Solberg (1936). Kuo (1954) examined the marginal stability threshold, extending Eady's work for a viscous, bounded, and non-hydrostatic (NHS) front, but found the temporal PDE to be analytically intractable. The growth rate of SI then was first explored at small to intermediate Richardson numbers by Stone (1966), generalising much of the work by Eady (1949), but still lacking dissipation and assuming hydrostatic motions. He found a stability criterion for SI that $Ri < 1$, and furthermore that SI dominates both KHI and baroclinic instabilities for $0.25 < Ri < 0.95$. Shortly thereafter, Stone (1971) reconsidered the NHS contribution, showing that the vertical inertia suppresses baroclinic and symmetric instabilities. Viscous contributions to the bounded NHS SI problem were only included by Weber (1980), approximated by a vertical pseudo-viscosity, as summarised in section 3.2.1.

We can develop an intuition for the mechanism permitting SI mode growth by revisiting the parcel theory introduced in section 2.1.3 for internal waves. In this same system which supports inertia-gravity waves, i.e. with both rotation and stratification, the absolute zonal momentum is still conserved, but now m surfaces are inclined due to the thermal wind shear:

$$m(x, z) = z\partial_x b / f + fx. \tag{7}$$

As m-surfaces are material, fluid parcels preferentially move along these slanted paths. Thus "slantwise convection" can occur if $\nabla_m b$ is gravitationally favourable for convection. Exactly equivalently, "slantwise inertial instability" occurs when the component of absolute vorticity normal to isopycnals is favourable, i.e. when $\omega_a \cdot \nabla b < 0$. Or in other terms, the variation of absolute momentum along isopycnal surfaces is negative (Taylor and Ferrari, 2009):

$$f\partial_x m|_\rho < 0. \tag{8}$$

Both of these instability criteria are equivalent to requiring anticyclonic PV. Schematically this means that the slope of isopycnals must be steeper than m-surfaces, and unstable SI modes will lie between these two.

In a geostrophically-balanced front, the SI stability criterion can be expressed as

$$Ri_g < \frac{f}{\zeta}. \tag{9}$$

For the infinite front we consider here, $\zeta = f$, and so through marginal control, SI would return the front to $Ri_g = 1$. For finite fronts, however, the vertical vorticity varies across the width of the front, breaking the symmetry and permitting the anticyclonic (buoyant) side of the front to remain symmetrically-unstable to a higher Ri_g. Finite fronts with large enough $\partial_x \bar{v}$, may also exceed the inertial instability threshold, $f\zeta < 0$, resulting in a hybrid SI and inertial instability (c.f. fig. 1 in Thomas et al. (2013)).

A number of observational studies in the past 20 years have built increasing evidence of the prevalence of SI in the dynamics of major frontal systems. The CLIvar MOde water Dynamics Experiment

(CLIMODE) project initiated in 2004, for example, was the first to notice that the Gulf Stream during the winter months commonly has negative PV in the surface boundary layer, indirectly suggesting that SI may be active (Marshall et al., 2009). Recently, Savelyev et al. (2018) even produced aerial images of SI in the North Wall of the Gulf Stream (c.f. fig. 2), which constitutes the hardest direct evidence of SI to date. Previous studies have indirectly attributed increased turbulence and dissipation (far exceeding that from atmospheric forcing) in anticyclonic PV regions to SI (Thomas et al. (2016) in the Gulf Stream, and D'Asaro et al. (2011) in the Kuroshio).

Work by Thomas et al. (2013) has greatly contributed to constructing a picture of the energetics of the major boundary currents. By analysing observations in the Gulf Stream, they determined the relative energetic contributions of SI and baroclinic instability, where measurements indicated consistently negative PV within the surface boundary layer. There they found indications that while baroclinic instability often precedes SI, both are crucial to efficiently dissipating the available potential energy from the Gulf Stream.

Parallel work has also focussed on regions where destabilising atmospheric forcing of the mesoscales — either by negative buoyancy fluxes (i.e. cooling) (Haine and Marshall, 1998; Thomas et al., 2013) or wind-stresses (Thomas and Lee, 2005) — could edge the front towards negative PV, and sustain "SI turbulence" and mixing stronger than what the forcing alone could generate (Joyce et al., 2009; Thomas and Taylor, 2010). This forcing takes the form of non-conservative fluxes on the RHS of the PV evolution equation (Thomas et al., 2013)

$$\frac{\partial q}{\partial t} = -\nabla \cdot \mathbf{J}, \tag{10}$$

where the flux is

$$\mathbf{J} \equiv \mathbf{u}q + \nabla b \times \mathbf{F} - (f\hat{\mathbf{k}} + \nabla \times \mathbf{u})\frac{Db}{Dt}. \tag{11}$$

2.3 Geostrophic Adjustment Theory

When the stable frontal setup described by the Eady model suddenly (on time-scales much shorter than the inertial period) loses the thermal wind shear that was once balancing baroclinic torques, the resulting geostrophic adjustment response is an attempt to regain a new balanced state. Rhines (1988) was the first to note that this adjustment process can result in inertial oscillations of the isopycnals. Rotunno and Thorpe (1989) showed that vertical fluxes of geostrophic momentum will tend to generate mean ageostrophic secondary circulations across the front, which as the turbulence decays, can explain the simple inertial oscillation of the mean flow that is left.

Precisely, the $\overline{v'w'}$ Reynolds stress component is responsible for exchanging low zonal momentum fluid with high momentum fluid above, and mixing down the thermal wind shear. Unbalanced dynamics such as SI contribute to this geostrophic momentum flux, and it will be shown to be important to understanding the details of the ensuing geostrophic adjustment.

The front evolution throughout geostrophic adjustment can be modelled by the inviscid hydrostatic equations. Tandon and Garrett (1994) considered a mixed layer initially in thermal wind balance, but which is then impulsively mixed (e.g. by a storm or SI) resulting in horizontally-invariant inertial oscillations. Following this perfect mixing of the geostrophic shear, the front undergoes inertial oscillations about the average steady-state position ($Ri = 1$). Because the inertial oscillations modulate the background stratification via the differential advection of buoyancy by the across-front velocity, then the time-oscillatory stratification can be found to evolve like

$$\partial_z b = M^4/f^2(1 - \cos ft). \tag{12}$$

The gradient Richardson number, however, remains constant throughout these oscillations:

$$Ri_g = \frac{\partial_z b}{(\partial_z u)^2 + (\partial_z v)^2} = 1/2. \tag{13}$$

Tandon and Garrett (1994) also considered the case when the vertical stratification is perfectly homogenised, but where the geostrophic shear is only partially mixed (with fraction s remaining). The gradient Richardson number then is found to be oscillatory,

$$Ri_g = \frac{(1-s)(1-\cos ft)}{s^2 + 2(1-s)(1-\cos ft)}, \tag{14}$$

and for $s > 0$, it is clear that at least a portion of the inertial oscillation has $Ri_g < 1/4$.

With no further internal sinks of energy, the background shear profile inertial oscillation would form a closed limit cycle. We will see that these inertial oscillations can excite further dynamics, such as shear instabilities, tertiary symmetric instability (Thomas et al., 2016), and parametric subharmonic instability (Thomas and Taylor, 2014), all of which further damp the inertial oscillation and help to equilibrate the front. We will also show that SI can provide this necessary geostrophic shear mixing needed to prompt geostrophic adjustment. We seek to quantify the mixing fraction, s, in section 3.3, as well as understand how viscous effects and turbulence in the inertial oscillation affect the evolution. A final extension to Tandon and Garrett (1994) that we will shed light on is the effect a finite mixing time has on the adjustment response and resulting oscillations.

2.4 Numerical Studies

It is quite often the case in global and regional models that scales smaller than the mesoscale are not fully resolved. At the same time, the evolution of the mesoscales depend on the details at these smaller scales — details such as turbulence dissipation, relevant transport quantities, or mixing, which in turn are sensitive to the structure of the submesoscales. Most commonly, instabilities which energise the submesoscales can generate large eddy transports, which without care go unmodelled in GCMs. There are important implications then for the parameterisations of turbulence and mixing in the upper ocean driven not only by boundary forcing, but also by internal sources such as these instabilities. This in part motivates the present investigation into SI and equilibration, and has driven many other local numerical process studies at the submesoscale. Haine and Marshall (1998) was the first to attempt to parameterise these vertical and lateral fluxes arising from various instabilities active in the mixed layer. Thomas et al. (2013) developed parameterisations to model the rate of energy extraction from the geostrophic flow in forced SI turbulence, and later at the sub-gridscale (Bachman et al., 2017).

A few previous numerical process studies of SI have investigated its nonlinear evolution with varying setups, but have focussed only on a single value of M^2/f^2 (Thomas and Lee, 2005; Taylor and Ferrari, 2009; Thomas and Taylor, 2010; Taylor and Ferrari, 2010). In particular, Taylor and Ferrari (2009) used a similar 2D frontal zone configuration to the present work with a stratified front having $M^2/f^2 = 42$, and found that the growing SI modes break down via secondary KHI, which further enhances PV fluxes into the domain, and ultimately stabilises SI. The present work simplifies these setups by using exactly the Eady problem, in order that focus be placed on the important changes in the nonlinear evolution with increasing front strength.

3 Methods

3.1 Governing Equations

Nondimensionalising the Boussinesq governing set for the Eady problem such that the thermal wind shear, M^2H/f, is unity in units where the vertical domain size, $H = 1$, brings out four dimensionless parameters:

$$\Gamma \equiv \frac{M^2}{f^2}; \quad Re \equiv \frac{H^2M^2}{f\nu}; \quad Ri \equiv \frac{N^2f^2}{M^4}; \quad Pr \equiv \frac{\nu}{\kappa}. \tag{15}$$

This problem setup emulates a local (and thus horizontally homogeneous) section of a front, and therefore lacks any lateral length-scale and explicit Rossby number. Rather, we use the frontal strength parameter, Γ, where it is understood that we could form a Rossby number given the aspect ratio, δ, as

$$Ro \equiv \frac{\omega_z}{f} = \frac{M^2}{f^2}\frac{H}{L} = \frac{\Gamma}{\delta}. \tag{16}$$

We will for simplicity reduce the parameter space by considering the most energetically-extreme case of vertical fronts (i.e. $Ri = 0$), and for a reasonable Reynolds number, $Re = 10^5$. This is all without much loss of generality, as the realised scalings have been shown to hold for larger Ri.

As is typical in the ocean, we assume a linear equation of state,

$$e' \propto b' \equiv -f\frac{\rho'}{\rho_0}, \tag{17}$$

and further take $b' \ll b_0$, so we can make the Boussinesq approximation. We consider changes in the Coriolis parameter to be small on these submesoscales, and so restrict the rotational dynamics to a

tangent f-plane. With these approximations, the nondimensionalised Boussinesq set is

$$\frac{D\mathbf{u}}{Dt} = -\nabla\Pi - \frac{1}{\Gamma}\hat{\mathbf{k}}\times\mathbf{u} + \frac{1}{Re}\nabla^2\mathbf{u} + b\hat{\mathbf{k}} \tag{18}$$

$$\frac{Db}{Dt} = \frac{1}{RePr}\nabla^2 b \tag{19}$$

$$0 = \nabla\cdot\mathbf{u}. \tag{20}$$

Here we've also ignored the non-traditional Coriolis acceleration component in the vertical momentum. The background basic state for linearisation and initial condition for the numerical simulations is

$$\begin{aligned}\bar{v} &= z\\ \bar{b} &= \Gamma^{-1}x + Ri\, z.\end{aligned} \tag{21}$$

Keeping in line with the Eady model as defined in section 2.1, we will also use solid horizontal boundaries at $z = 0$ and 1 which are taken to be insulating and stress-free (Eady, 1949).

3.2 Linear Stability Analysis

3.2.1 Primary SI Approximations

By restricting the scope of this work solely to SI and the local modelling of finite fronts, we must then restrict the regime of interest to $\Gamma \approx [1, 100]$. Any smaller than $\Gamma = 1$, and baroclinic instability would dominate growth on the basic state (21). Similarly, for fronts stronger than $\Gamma = 100$, the width of the finite front we are emulating could become comparable to the Rossby deformation radius, and would have a non-negligible effect on the dynamics. This question of the effect of finite support on SI and baroclinic instability modes will be reserved for future work.

Many past studies have considered the stability and dispersion relation for symmetric instability under varying approximations. Solberg (1936) was first to define the stability criterion for SI, and worked out the dispersion relation for a vertically-unbounded, inviscid front under the hydrostatic approximation. However, because vertical motions are often quite large in frontal regions the hydrostatic approximation is not particularly sound. Ren (2008) recently reviewed the characteristic differences among modes in limiting cases for bounded versus unbounded non-hydrostatic SI dispersion, but critically has left out the regularising effect of dissipation, invalidating much of the asymptotic argument at high wavenumber. The following thus determines the dispersion of a bounded and viscous front without requiring the hydrostatic assumption.

We begin by linearising the Boussinesq set, (18-20) about the Eady basic state (21). The most unstable perturbations are two-dimensional (Stamper and Taylor, 2016), and so we can greatly simplify the linear equations by considering linear perturbations restricted to the x-z plane:

$$\begin{aligned}\partial_t u &= -\partial_x\Pi + \frac{1}{\Gamma}v + \frac{1}{Re}\nabla^2 u\\ \partial_t v + u\partial_x\bar{v} + w\partial_z\bar{v} &= -\frac{1}{\Gamma}u + \frac{1}{Re}\nabla^2 v\\ \partial_t w &= -\partial_z\Pi + \frac{1}{Re}\nabla^2 w + b\\ \partial_t b + u\partial_x\bar{b} + w\partial_z\bar{b} &= \frac{1}{RePr}\nabla^2 b\\ 0 &= \nabla\cdot\mathbf{u}.\end{aligned} \tag{22}$$

As is typical in many stability analyses, we transform this set of PDEs into a set of ODEs by further assuming normal mode perturbations autonomous in x of the form

$$\chi(x, z, t) = \hat{\chi}(z)\exp(i(kx - \omega t)) \tag{23}$$

where the eigenfunction, $\hat{\chi}(z)$, must then be chosen to satisfy the relevant boundary conditions. The set (22), after substitution and simplification using the streamfunction defined by $\mathbf{u} = \nabla\times\psi\hat{\mathbf{j}}$, becomes

$$\left(i\omega + \frac{1}{Re}\left(-k^2 + D^2\right)\right)^2\left(-k^2 + D^2\right)\hat{\psi} = \left(-\frac{1}{\Gamma^2}D^2 - \frac{2ik}{\Gamma}D + k^2 Ri\right)\hat{\psi}, \tag{24}$$

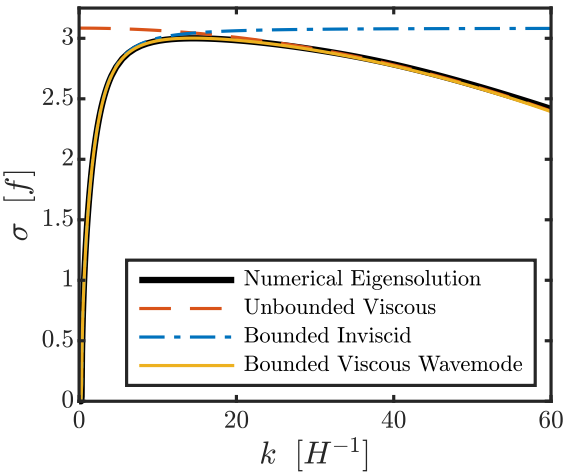

Figure 5: The dispersion relation for SI of a vertical front with $\Gamma = 10$ and $Re = 10^5$. The frequency of the SI modes are everywhere 0 except where linearly stable at very small wavenumber.

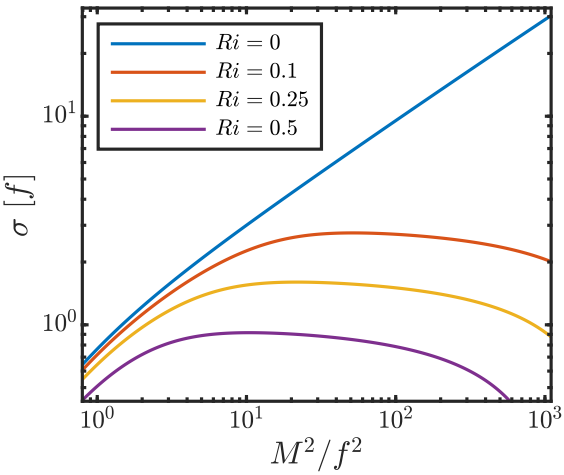

Figure 6: The growth rate of the fastest growing SI mode ($n = 1$) and wavenumber at $Re = 10^5$, for the vertical front ($Ri = 0$) and for increasing stratification, as a function of Γ.

where $D \equiv \mathrm{d}/\mathrm{d}z$ for notational ease. The new boundary conditions for $\hat{\psi}$ on this 6$^{\text{th}}$ order ODE are

$$\begin{aligned} \hat{\psi} &= 0 \\ D^2\hat{\psi} &= 0. \end{aligned} \tag{25}$$

To render this system analytically tractable, we can approximate equation (24) as a 2$^{\text{nd}}$ order ODE just by writing the vertical diffusion terms as spatially-invariant wave modes (Weber, 1980),

$$D^2\hat{\psi} \approx l^2\hat{\psi}. \tag{26}$$

Equation (24) then becomes

$$\left[\left(i\omega - \frac{1}{Re}\left(k^2+l^2\right)\right)^2 + \Gamma^{-2}\right] D^2\hat{\psi} + \frac{2ik}{\Gamma} D\hat{\psi} - k^2\left[\left(i\omega - \frac{1}{Re}\left(k^2+l^2\right)\right)^2 + Ri\right]\hat{\psi} = 0, \tag{27}$$

which has eigensolutions of the form

$$\hat{\psi} = \exp(i\lambda_1 z) - \exp(i\lambda_2 z) \tag{28}$$

that match the boundaries if $\lambda_1 - \lambda_2 = 2\pi n$, for the chosen eigenmode number, n. Equation (27) is thus reduced to a quadratic eigenproblem which may be solved by simple numerical iteration while enforcing the viscous wave-mode approximation that

$$D^2\hat{\psi} = \frac{1}{2}\left(\lambda_1^2 + \lambda_2^2\right) \approx l^2\hat{\psi}. \tag{29}$$

The exact 2D numerical eigensolution to the linear set (22) was also computed using a pseudo-spectral eigenvalue solver written in `Matlab`. The computed solutions to (27) give good agreement with this numerical solution, as shown in figure 5. This new solution correctly accounts for both the limiting effects of the vertical boundaries at low wavenumber, and of viscosity at high wavenumber. Accurate in the low wavenumber limit, Stone (1971) determined this inviscid, bounded solution, where the mode growth becomes suppressed as it feels the constraint of the boundaries for $k \lesssim 2\pi/H$. In the other limit, Taylor and Ferrari (2009) writes the viscous, but unbounded dispersion relation for hydrostatic motions, which due to the $-|\mathbf{k}|^2$ viscous decay, has maximum growth for $k = 0$. The structure of the exact ($n = 1$) viscous, bounded eigenfunction ($\hat{u}$) is shown in the background of figure 10. It is due to both viscous and non-hydrostatic effects that these linear SI modes are no longer parallel to isopycnals as they were in e.g. Stone (1966).

We can now take the fastest-growing solution mode to (27) and consider how it scales across Γ. While there is a nearly $\sigma/f \propto \sqrt{\Gamma}$ trend for the vertical front, stratification apparently has a larger impact

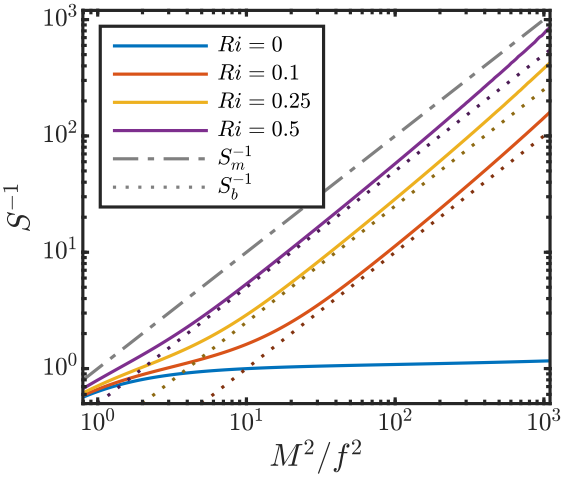

Figure 7: The fastest growing eigenmode *inverse* slope scaling with front strength, and for increasing background stratification. The unstable SI mode inclination must remain between the absolute momentum (s_m) and isopycnal (s_b) slopes, which for $Ri = 0$, $s_b^{-1} = 0$. For stronger fronts, the modes diverge from isopycnals as they become increasingly flat, but asymptote to 1 in the unstratified, inviscid case.

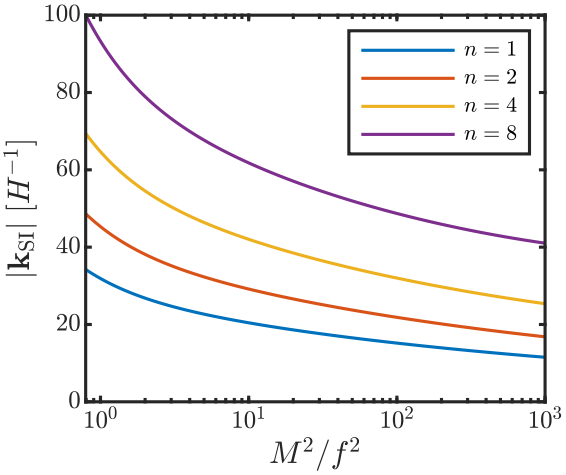

Figure 8: The fastest growing SI mode wavenumber for $Ri = 0$ and various mode numbers.

on strong fronts, as seen in figure 6. While the SI modes must still be between isopycnals and absolute momentum surfaces to extract energy (figure 7), we see that with increasing viscosity and decreasing front strength, modes rather approach the absolute momentum surfaces. This permits a larger buoyancy production of energy, as shown in figure 9, but which nevertheless is dominated by geostrophic shear production, $\mathcal{P}$, in the rest of the regime.

3.2.2 Secondary Shear Instability

The linear growth of Symmetric Instability alas does not go unchallenged. Eventually, the shear induced by the SI modes themselves roll up, and prompt transition to turbulence. The critical amplitude at which the SI modes themselves become unstable (i.e. when $\sigma_{\mathrm{KH}} \approx \sigma_{\mathrm{SI}}$) must then be determined. A secondary numerical linear stability analysis of the combined Eady and growing SI mode basic state is computed in the rotated coordinates shown in figure 10, and which is used to compute the critical amplitude, U_c, as plotted in figure 11.

We formulate the 1D linear KH stability problem using a sinusoidal extension of the structure of the full SI eigenfunction (evaluated at the mid-plane) in the rotated domain. This new basic state now has components of the background horizontal stratification as well as the induced stratification from the SI modes themselves. We employ a similar pseudo-spectral solver as in section 3.2.1, to compute the critical SI mode amplitude, U_c, which ultimately marks the end to linear SI growth.

While it is true that the most unstable SI wavenumber, $|\mathbf{k}_{\mathrm{SI}}|$, increases as n and Re increases, still the scaling remains the same because U_c is dominated by the scaling of σ_{SI}. This is demonstrated in figure 11 where the classic KHI scaling analysis (i.e. neglecting the buoyancy eigenmode component and rotated gravity component) is shown alongside these results for U_c. The dashed lines here show the scaling achieved when assuming $\sigma_{\mathrm{KH}} \propto |\mathbf{k}_{\mathrm{SI}}| U_c$ along with the SI growth rate in the limit of large Γ, $\sigma_{\mathrm{SI}}/f \propto \sqrt{\Gamma}$, for inviscid, bounded SI. The range of validity of this scaling,

$$\frac{U_c}{HM^2/f} \propto (H|\mathbf{k}_{\mathrm{SI}}|\sqrt{\Gamma})^{-1} \tag{30}$$

(in units of the thermal wind shear) can be understood by constructing an indicative KHI Rossby number, with $U_{\mathrm{SI}} = U_c$:

$$Ro_{\mathrm{KH}} = \frac{U_{\mathrm{SI}}}{L_{\mathrm{SI}} f} = \sqrt{\Gamma}. \tag{31}$$

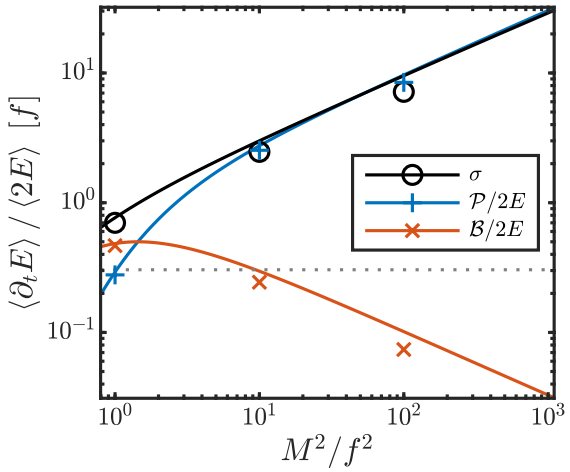

Figure 9: Contribution of the most unstable linear SI mode to the energy budget for $Re = 10^5$. Normalised by the kinetic energy, the geostrophic shear production and buoyancy flux are relatable to the growth rate, σ. As expected with SI, the instability still primarily draws energy from the thermal wind shear into the kinetic energy of the mode through the KE production term. The grey dotted line indicates the growth rate of baroclinic instability for this choice of parameters.

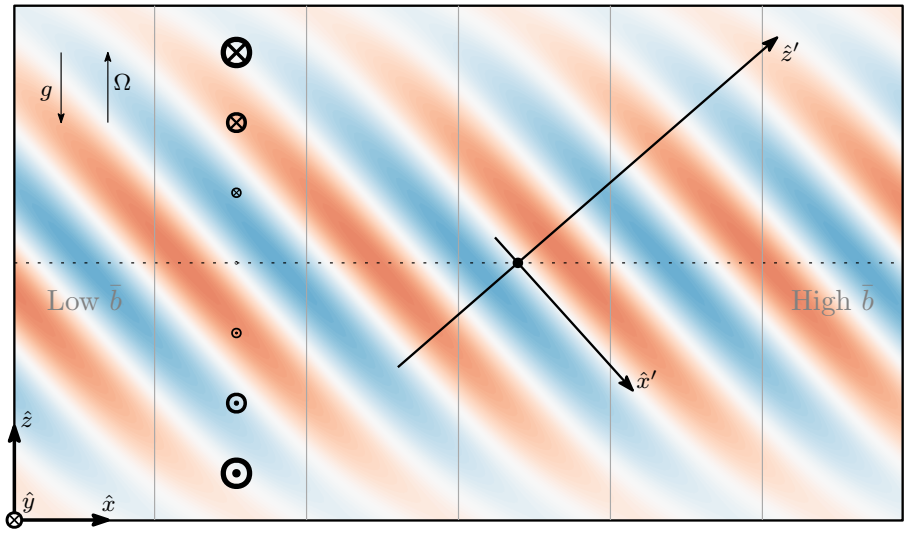

Figure 10: Diagram showing the secondary stability analysis coordinate transformation drawn over the linear SI mode (u). The primary SI basic state is also indicated, with grey isopycnal lines showing the linearly increasing buoyancy from left to right, as well as the thermal wind vectors into the page which balance the baroclinic torques.

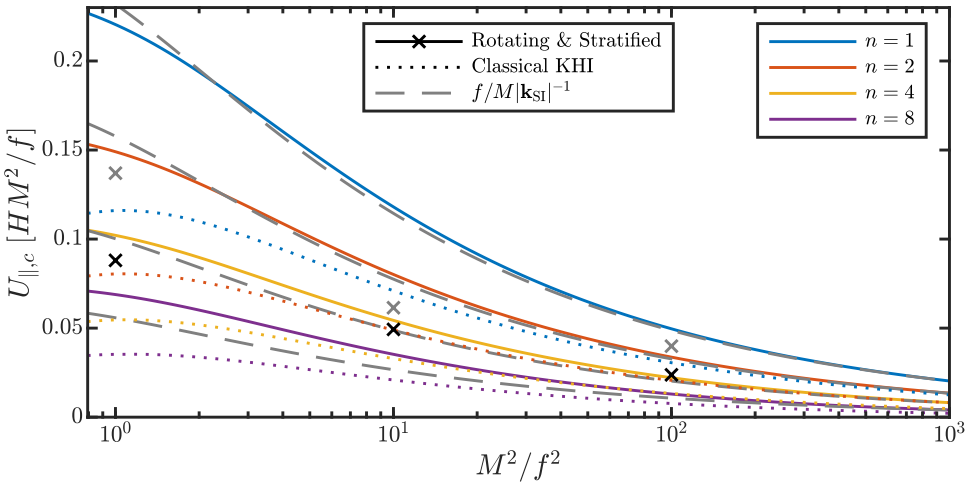

Figure 11: The critical amplitude of the most unstable SI mode at which secondary instability begins to dominate, shown in units of the thermal wind. Dotted lines show this critical amplitude when non-traditional KH contributions (rotation & stratification) are neglected. Black symbols show the amplitude at τ_c in 2D simulations, and grey symbols show the mean RMS velocity over the first 10 inertial periods. Due to weak scale and mode selection, these simulations contain a range of n and k_x, both of which break down to shear instability more quickly than for $n = 1$ shown.

This explains the importance of non-traditional effects such as rotation on the KHI analysis for $\Gamma \lesssim 10$.

The critical SI mode amplitude can be extracted from numerical simulations, and is indicated with black x's in figure 11. The initial noise used in these simulations projects onto a range of n and k, but near transition, it is the higher n modes present that will break down first (because they have larger k_{SI}, and thus a lower U_c). Regardless of the exact amplitude being more representative of a "mean" $n \approx 5$ (weakly varying with Γ), the scaling shown still holds.

3.2.3 Tertiary SI

Following SI growth and breakdown by KHI into turbulence, the now geostrophically-unbalanced front begins inertially oscillating as described in section 2.3. Thomas et al. (2016) performed a linear stability analysis on the time-oscillatory basic state of a front undergoing inertial oscillations. Although Floquet analysis results in a PDE which is both analytically and numerically intractable, Thomas et al. (2016) rather seeded this time-dependent basic state with the most unstable SI mode from classical theory, and observed the resulting transient growth. They found periods of explosive growth corresponding with times when the front is minimally stratified, implying greatly increased turbulence generation and thus dissipation. In a turbulent front, however, the effective turbulent viscosity can be many times larger than the molecular viscosity, and has the effect of selecting a larger preferred wavelength for these tertiary SI modes.

3.3 SI Linear Mode Transport

In light of these stability analyses, the natural question to ask is: What impact does the linear SI phase and ensuing turbulence have on the resulting evolution, and how does it depend on the strength of the front? To do this, we combine the results of sections 3.2.1 and 3.2.2, to determine the cumulative effect that SI contributes leading up to the breakdown of these coherent modes at τ_c — the time when SI has grown to U_c. This analysis will indicate the importance of the linear modes for setting the amount of transport and thus the size of the resulting inertial oscillations.

With the complex eigenfunction, $\hat{\psi}$, found by iteratively solving for λ_1 and λ_2 in equation (28), we can then determine the full structure of these modes: $\hat{u}$, $\hat{v}$, $\hat{w}$, and $\hat{b}$. With these, we compute the correlations relevant to the transport and energetics of the development of SI. We first must normalise each of the modes by $\sqrt{|\hat{u}|^2 + |\hat{v}|^2}$, and then rewrite them in the normal mode form, (23), using the parameter and eigenvalues of equation (27).

We first consider the contributions to the turbulent kinetic energy (TKE) equation. The TKE,

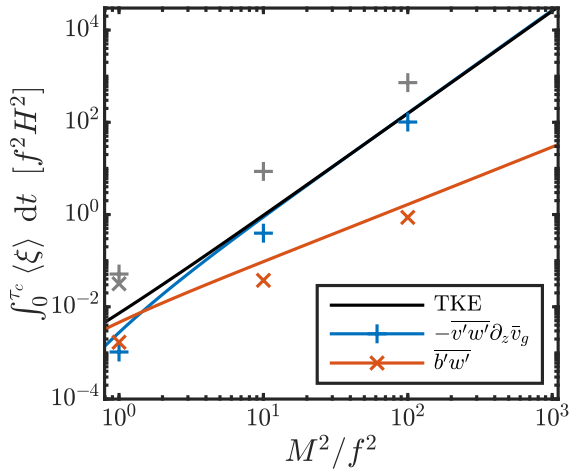

Figure 12: The cumulative KE budget contributions from the $n = 1$ linear SI mode, integrated through U_c. Coloured symbols show the value derived from the 2D simulations, and grey symbols show the time-integral over the first 10 inertial periods. Due to weak scale and mode selection, these simulations contain a range of n and k_x, yet with increasing frontal strength the values calculated from the simulations approach the $n = 1$ line shown due to stronger mode selection as the higher modes are damped by viscosity.

$1/2\,\langle u_i' u_i' \rangle$, in this problem evolves like

$$\frac{\partial}{\partial t}\left(TKE\right) = \underbrace{-\left\langle \overline{u'w'}\frac{\partial \bar{u}}{\partial z}\right\rangle}_{-\mathcal{P}_x} \underbrace{-\left\langle \overline{v'w'}\left(\frac{\partial \bar{v}_a}{\partial z}+\frac{\partial \bar{v}_g}{\partial z}\right)\right\rangle}_{-\mathcal{P}_y} + \underbrace{\langle w'b'\rangle}_{\mathcal{B}} \underbrace{-\frac{1}{Re}\left\langle \frac{\partial u_i'}{\partial x_j}\frac{\partial u_i'}{\partial x_j}\right\rangle}_{\varepsilon}. \tag{32}$$

Here, $\langle\cdot\rangle$ indicates a volume average over the entire domain. The first two terms on the RHS represent the shear production, $\mathcal{P}$, converting energy from the mean flow into TKE. Specifically, the along-front contribution is split into a geostrophic shear production term, $\mathcal{P}_g$, energised by the thermal wind shear, and an ageostrophic part. The other potential source of TKE comes from buoyancy production, $\mathcal{B}$, which represents the transfer of energy from PE into TKE.

The cumulative generation of TKE by each of these terms for $n = 1$ in (32), integrated from $t = 0$ up to transition at τ_c is shown in figure 12. As expected for SI, the contribution from $\mathcal{P}_g$ exceeds $\mathcal{B}$, except for small Γ, where baroclinic instability may begin to compete. Interestingly, even for these SI modes that are very flat (i.e. inclined to the isopycnals) in strong fronts, the energetics are still dominated by geostrophic shear production which relies on the mode vertical velocity to exchange geostrophic momentum.

We consider now the primary terms in dominant balance in the mean momentum equation. Subtracting off the background, geostrophic velocity and buoyancy gradient from the Boussinesq equation (18), then the resulting system is horizontally-autonomous, so we can Reynolds average in the x and y directions (denoted by $\bar{\cdot}$). After using continuity and the averaged buoyancy equation, the ageostrophic Reynolds-averaged Navier–Stokes (RANS) equations are

$$\partial_t \bar{u}_a + \partial_z \overline{u'w'} = \Gamma^{-1}\bar{v}_a \tag{33}$$

$$\partial_t \bar{v}_a + \partial_z \overline{v'w'} = -\Gamma^{-1}\bar{u}_a. \tag{34}$$

To determine the dominant balance at early times, we make the ansatz that the Coriolis term in equation (34) is small, and construct the ratio

$$\frac{-\partial_z \overline{u'w'}}{\Gamma^{-1}\bar{v}_a} \approx 2\Gamma^2\sigma^2\frac{\lambda_1+\lambda_2}{2k\Gamma-\lambda_1-\lambda_2} \tag{35}$$

and similarly for the terms in the y-momentum equation,

$$\frac{-\partial_z \overline{v'w'}}{-\Gamma^{-1}\bar{u}_a} \approx 2\frac{2k\Gamma-\lambda_1-\lambda_2}{\lambda_1+\lambda_2}. \tag{36}$$

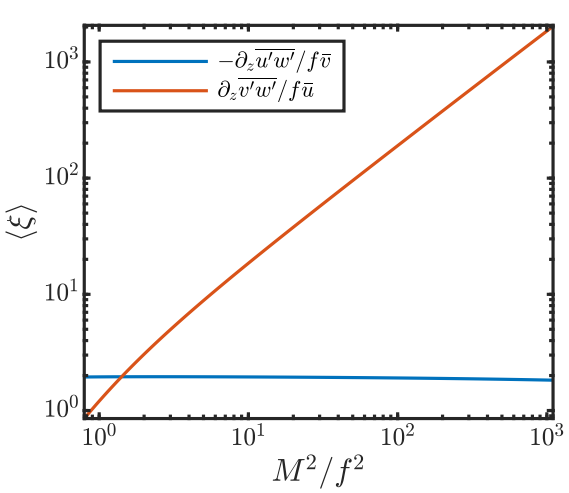

Figure 13: The ratio of the Reynolds Stress and the mean Coriolis term in each of the x- and y- momentum equations, shown for the fastest growing SI eigenmode. The approximation for the Coriolis term in the denominator is self-consistent with the dominant balance of Reynolds stresses shown, and which agrees with that observed in the simulations following.

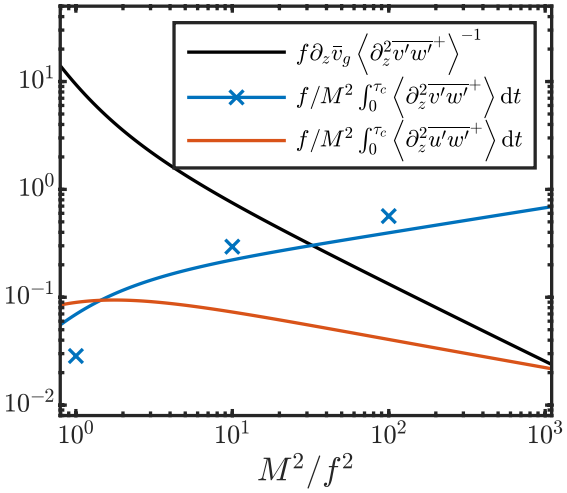

Figure 14: The cumulative linear SI mode contributions to the vertical gradient of the x and y ageostrophic momentum equations, integrated through U_c, with symbols showing the extracted values from the 2D simulations. Momentum is only rearranged within the domain by the linear modes, and so the domain average is conditioned on positive fluxes. The time-scale to entirely mix the thermal wind shear is also shown in black.

Each of these expressions, plotted in figure 13, are self-consistent only if both ratios are $\gg 1$. This is indeed the case in the regime of interest, $\Gamma \gtrsim 1$, and so we can conclude that the mean ageostrophic y-momentum is driven more strongly than the x-momentum, so that the dominant balance is initially

$$\partial_t \bar{v} \approx -\partial_z \overline{v'w'}. \tag{37}$$

While we can determine the dominant balance through the linear contributions to the RANS equations, to understand the loss of geostrophic balance we must consider the vertical derivative of the y-momentum equation. Similarly to the TKE equation, we compute the SI mode cumulative vertical gradient of momentum fluxes through τ_c, shown in figure 14. The units are chosen such that the integrated $\partial_z^2\overline{v'w'}$ term can be interpreted as the fraction of the thermal wind shear which is mixed down by the linear SI mode alone — precisely the fraction, s (Tandon and Garrett, 1994)! We see with increasing front strength, the linear SI modes are able to remove a larger fraction of the thermal wind shear before τ_c, and for large M^2/f^2 scales like $\Gamma^0.25$. Furthermore, the thermal wind shear destruction time-scale (in black) for these stronger fronts becomes considerably less than f^{-1}, indicating that the front cannot immediately respond by slumping in a quasi-balanced manner. Specifically, these disparate time-scales in strong fronts means that a more nearly geostrophic adjustment process ensues. This is contrasted with weaker fronts where these time-scales are comparable, and so there is a less energetic quasi-balanced adjustment.

3.4 Numerical Model

We have employed the non-hydrostatic hydrodynamics code, `diablo`, to extend these linear analyses and study the nonlinear evolution to equilibration of fronts with varying strength. `Diablo` solves the fully non-linear Boussinesq equations on an f-plane with a modified constant Smagorinsky subgrid-scale model (Taylor, 2008). Second-order finite differences in the vertical and a collocated pseudo-spectral method in the horizontal directions are employed, along with a third-order accurate implicit-explicit time-stepping algorithm using Crank-Nicolson and Runge-Kutta with an adaptive step size.

In the present study, we consider but a small segment of a finite front, which allows us to approximate this local section by a horizontally-homogeneous domain. We further restrict the parameter space of Γ and consider emulating relatively narrow fronts so that baroclinic instability can be ignored in the present study. This validates our study of the linear and nonlinear evolution of these fronts in 2D.

Run	M^2/f^2	L_x/H	L_y/H	L_{BI}/H	L_{SI}/H	N_x	N_y	N_z	$\tau_c f$
R1_2D	1	4	–	3.97	0.23	2048	1	512	14.0
R10_2D	10	16	–	39.74	0.43	4096	1	512	2.33
R100_2D	100	64	–	397.38	0.61	16384	1	512	0.49
R1_3D	1	4	0.25	3.97	0.23	512	32	256	14.0
R10_3D	10	16	0.25	39.74	0.43	2048	32	256	2.33

Table 1: Summary of the parameters and details of the presented numerical simulations.

We later present the results of short 3D large-eddy simulations to show that these results are robust in three dimensions. However, to exclude baroclinic instability effects in the along-front direction, we take $L_y = 1/4$, which is slightly larger than the typical turbulence correlation length, but is smaller than the baroclinic waves.

4 Results

4.1 Numerical Simulations

Each of the 2D simulations with $\Gamma = \{1, 10, 100\}$ were run for 100 inertial times, except for the $\Gamma = 100$ case which could only run until $tf = 40$. In addition to the computational cost scaling as Γ^2 due to the requirement for a shorter time-step and a larger domain, the large aspect ratio of the domain ($L_x \sim \mathcal{L}_d \sim \Gamma$) means that the additional computation is not easily parallelised.

Each simulation is initialised as a balanced, vertical front (21), with uniform spectral noise added to the momentum field with amplitude 10^{-4}. We do not vary the Reynolds number across experiments, which is held at $Re = 10^5$ to give a reasonable approximation to oceanic values. A vertical resolution of 10 times the Kolmogorov scale, $\eta \sim Re^{-3/4}$, then is used in each simulation, and which is sufficient to resolve the range of unstable SI wavenumbers, as well as capturing much of the inertial range of turbulence. Many of the other parameters and details of each of the runs are summarised in table 1.

The simulations have helped to paint a picture of these frontal energetics — from SI and KHI-generated turbulence, to PE release by geostrophic adjustment, tertiary SI, and further shear instabilities towards equilibration. While the details may vary slightly depending on Γ, three distinct phases seem to be quite generic in frontal regions:

1. Linear growth (shown across the top row of figure 15), energises a broad wavenumber spectrum (apparent in figure 16) due to the weak scale (k) and mode (n) selection of SI from the initial spectral noise. This means rather that a range of wavenumbers and modes will be represented, and combine to contribute to the SI mode transport and dynamics, the predictions of which still appear to be remarkably consistent. For example, figure 9 shows the linear growth and TKE budget terms extracted from the simulations in the linear phase.

2. As the linear SI modes reach U_c, their self-induced shear KHI converts much of this coherent energy into TKE (shown across the middle row of figure 15). The linear SI and turbulence removes energy from the background geostrophic shear flow (shown as +'s in figure 12), and sets into motion large-scale inertial oscillations.

3. The resulting geostrophic adjustment briefly excites tertiary SI (with larger wavelength because ν_t is large), which consequently becomes KHI unstable (bottom row of figure 15). The generated turbulence and enhanced mixing during adjustment increases PV fluxes into the domain, which allows the ageostrophic circulation to restratify the front, eventually to $Ri_g = 1$. Once the mean $fq > 0$, SI is neutralised, leaving fossil oscillations (apparent in figure 16) which continue to hold and extract energy.

4.1.1 Geostrophic Adjustment

We now analyse the nonlinear behaviour as the front loses balance, and how the adjustment response and inertial oscillation amplitude depends on the front strength (and s, as in Tandon and Garrett (1994)). Consider first the turbulent momentum balance described by equation (34) on a particular horizontal plane, $z = 3/4$. The linear analysis (37) predicted an initial dominant balance whereby $\partial_z \overline{v'w'}$

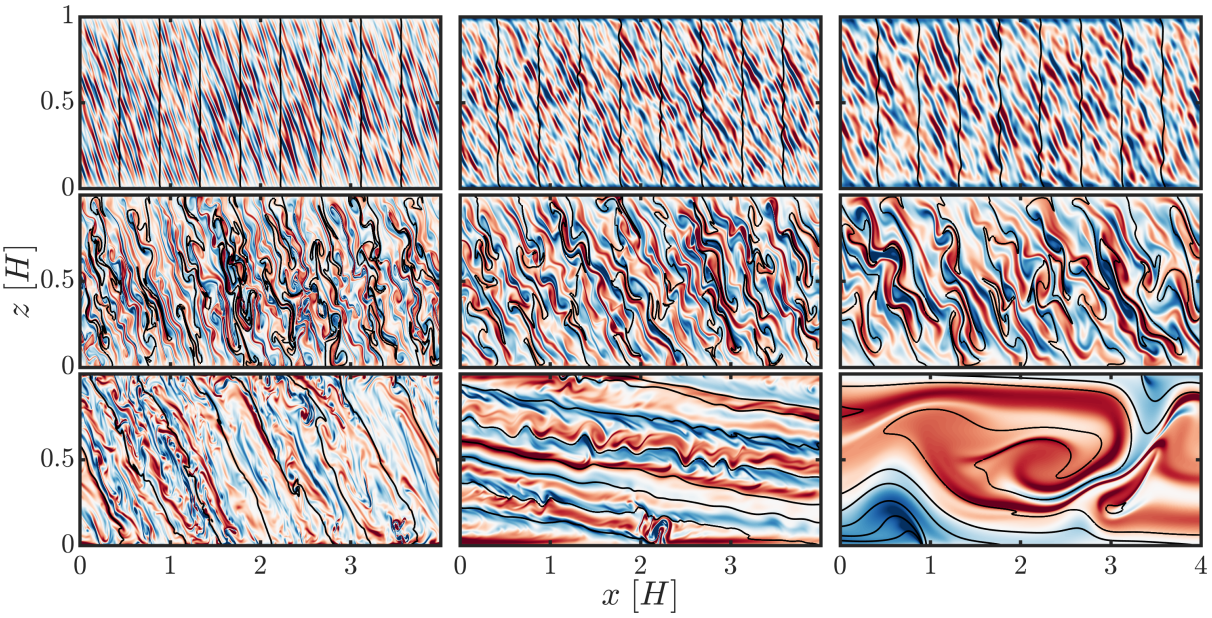

Figure 15: Slices across the front comparing the normalised along-front vorticity, ω_y, with buoyancy contours, for $\Gamma = 1$ (left), 10 (centre), and 100 (right). Three times are shown (from top to bottom) starting in the linear regime, then when secondary shear instability becomes active, and finally at late times when tertiary SI develops and subsequently rolls up into Kelvin-Helmholtz instability. Note that only a subset of the horizontal domain is shown for both $\Gamma = 10$ and 100.

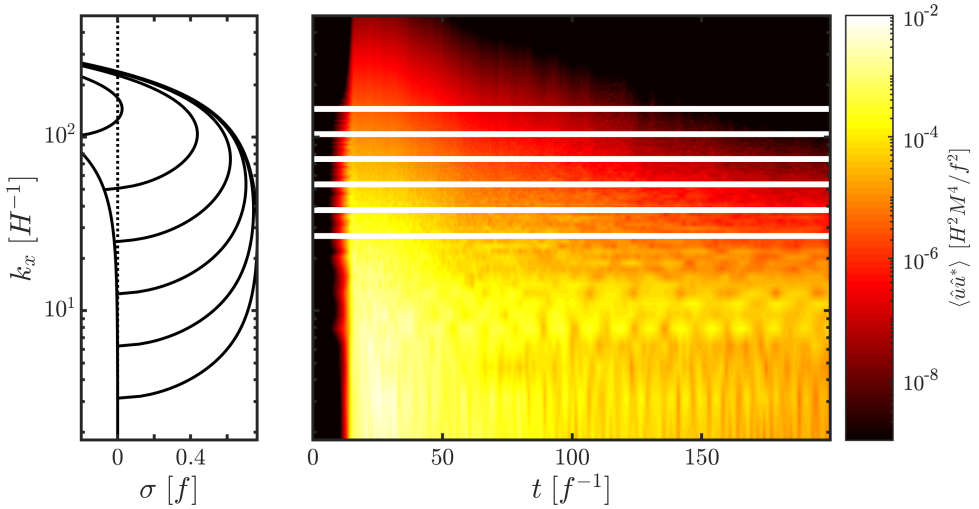

Figure 16: Time-series of the across-front wavenumber (right), along with the dispersion relation for $n = 1, 2, 4, 8, 16, 32$ (left) for the 2D $\Gamma = 1$ simulation. Wavenumbers of peak growth are indicated with horizontal white bars. Remnants of the signal of secondary SI with larger wavelength (due to larger effective viscosity) is apparent at later times. Subinertial oscillations around $k_x = 8$ are also visible.

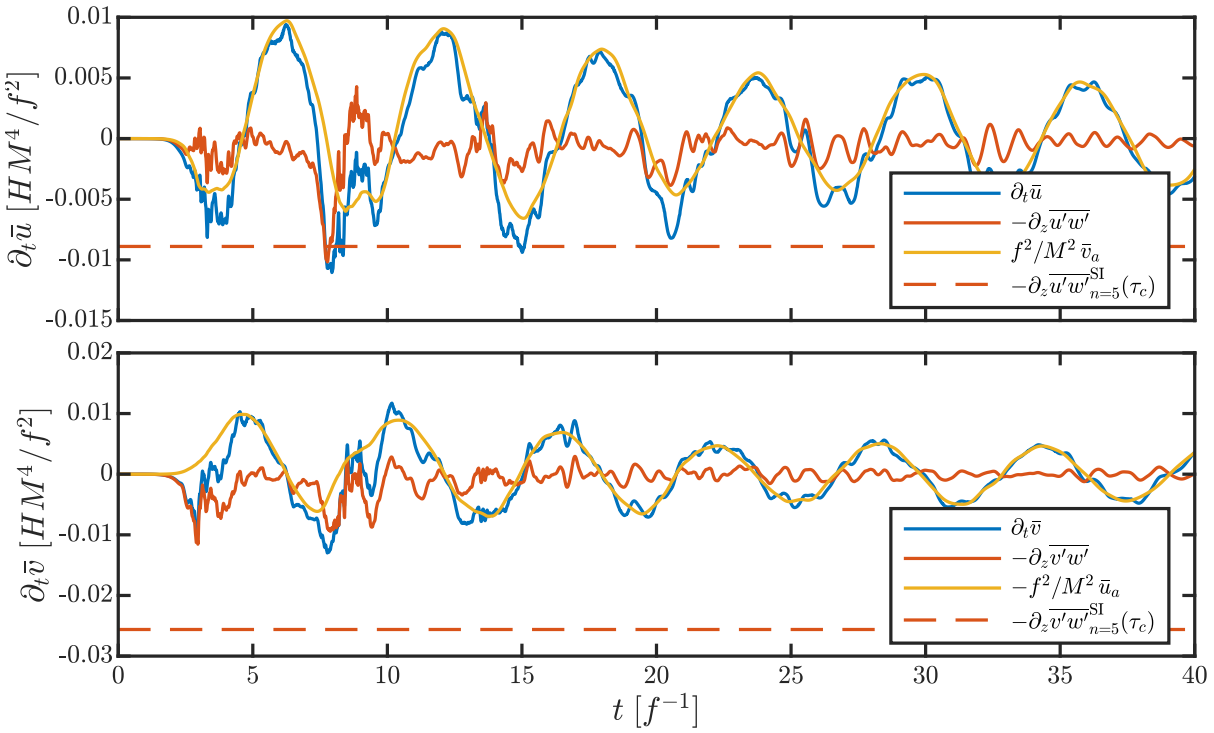

Figure 17: Horizontally-averaged momentum budget at $z = 3L_z/4$ for $\Gamma = 10$. An exchange of the dominant RANS balance in the along-front momentum (lower) is apparent following the initial SI growth and transition to turbulence. The linear SI mode transport at turbulent transition is also shown.

is responsible for destabilising the front (contributed by both linear modes and turbulence). In the model example for $\Gamma = 10$ (shown in figure 17) it is clear that indeed this Reynolds stress term is driving the ageostrophic y-momentum until $tf \approx 4$ at which point it has induced geostrophic adjustment. Around $tf = 5$, the dominant balance in the RANS equations is exchanged and becomes

$$\partial_t \bar{\mathbf{u}} \approx -\Gamma^{-1} \hat{\mathbf{k}} \times \bar{\mathbf{u}} \tag{38}$$

from the large-scale inertial oscillation.

In each of the three cases, it is interesting to note that during the exchange of dominant balance from Reynolds stress-driven ageostrophic motions, to the balanced motions assumed in the theory of Tandon and Garrett (1994), we see a brief slowdown at $Ri_g = 1/2$ (figure 19). Tandon and Garrett (1994) indeed predicted this constant value of Ri_g for inviscid adjustment as shown in equation (13). However, viscous effects and further PV fluxes permit the onward increase towards equilibration at $Ri_g = 1$.

To further emphasise the difference in the nonlinear evolution of the front following vertical mixing, we can examine hodographs of an averaged measure of the mean velocity gradient. Consider the domain averages, $\langle \bar{u} \rangle$ and $\langle \bar{v} \rangle$, constructed by rectifying the 0-mean shear profiles:

$$\langle \bar{u} \rangle = \frac{1}{L_z} \left[-\int_0^{L_z/2} \bar{u}(z)\, \mathrm{d}z + \int_{L_z/2}^{L_z} \bar{u}(z)\, \mathrm{d}z \right] \tag{39}$$

and similarly for $\langle \bar{v} \rangle$. Plotting these two quantities in $\langle \bar{u} \rangle$-$\langle \bar{v} \rangle$ phase space, then an inertial oscillation of the front traces a circle. This is shown in figure 20, where the axes are in units of the thermal wind shear, and so the initial condition is at $(0, 1)$.

Starting at $t = 0$ (designated with a circle), each of the three fronts depart from the geostrophic balance fixed point and begin tracing inertial trajectories. However, depending on the strength of the front, the details of the adjustment greatly differ. For a weak front ($\Gamma = 1$, left pane), inertial adjustments occur faster than SI growth. The resultant quasi-balanced evolution of the front as it slowly slumps is evident as $\langle \bar{v} \rangle$ remains nearly geostrophically-balanced at 1, whereas $\langle \bar{u} \rangle$ is driven by the Reynolds stresses from SI and turbulence. This is contrasted with the stronger front, where vertical fluxes rapidly (relative to the inertial time-scale) mix down the geostrophic shear before inertial effects can influence the mean dynamics, and which is apparent by the departure from $\langle \bar{v} \rangle = 1$. The strongest front mixes down $\langle \bar{v} \rangle$ to

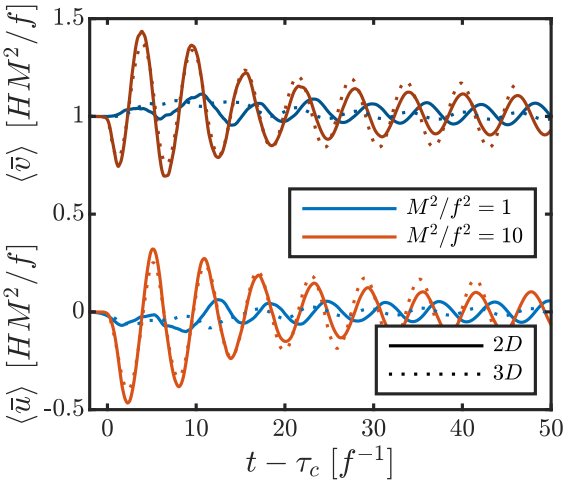

Figure 18: Comparison of the mean total u and v for the 2D and 3D simulations. While the amplitude of the decaying inertial oscillations varies slightly, the general behaviour is robust in 2D.

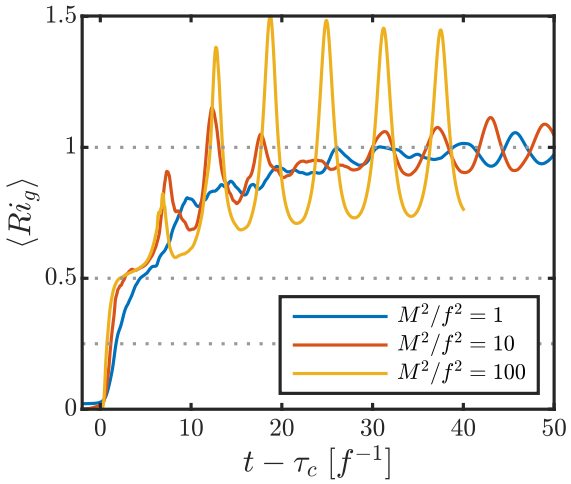

Figure 19: Gradient Richardson number for each of the three runs shows increasingly fast restratification for stronger fronts. SI ultimately stabilises the front, taking it to a mean Richardson number of 1.

nearly half of the initial value before any inertial response occurs. This distinct separation of timescales for large Γ more closely matches the assumptions required in Tandon and Garrett (1994).

These observations agree with our prediction in section 3.3. Blue x's in figure 14 show the amplitude of the thermal wind shear at τ_c extracted from simulations. Consistent with this picture, we see that for $\Gamma \gtrsim 10$ the time required to fully mix down the thermal wind shear is less than an inertial period, thus indicating a more abrupt geostrophic adjustment.

Robustness in 3D We check the robustness of our results from the presented 2D results using two 3D runs with $\Gamma = 1$ and 10. Excluding possible mixed baroclinic-symmetric modes, as found in numerical simulations by Stamper and Taylor (2016), we conclude that the along-front dynamics are not important to the resulting inertial oscillations, as compared in figure 18.

4.1.2 Energetics

We can understand a lot about the energetics of this system by considering where energy is initially stored as well as how it's accessed. The obvious source of energy which initially generates turbulence via the geostrophic shear production of SI is the background geostrophic flow kinetic energy. In our chosen dimensionless units, the kinetic energy of the geostrophic flow is $KE_b = 1$. While the equilibrated state (also in geostrophic balance) has the same mean kinetic energy, the intermediate unbalanced state following mixing of the thermal wind shear can temporarily release an amount of energy,

$$\Delta KE = \frac{1}{3}(1 - s^2). \tag{40}$$

The background constant stratification, $\partial_x \bar{b}$, held by this local model also presents a reservoir of potential energy. The PE available for SI to extract is defined relative to the lowest state that SI can take the front to, being $Ri_g = 1$. Thus, in geostrophic units,

$$PE = \frac{1}{3}\left(1 - \partial_z \bar{b}\right), \tag{41}$$

so similarly a maximum of $\Delta PE = 1/3$ (in geostrophic shear units) can be accessed and released by SI.

We can see these reservoirs interacting and exchanging energy in the example budget summary for $\Gamma = 10$, shown in figure 21. Initially geostrophic shear production via SI energises TKE by extracting energy from the mean kinetic energy (MKE), in the thermal wind shear. This production is split between turbulent dissipation and the MKE_a,

$$1/2 \left\langle \bar{u}_{i,a} \bar{u}_{i,a} \right\rangle \tag{42}$$

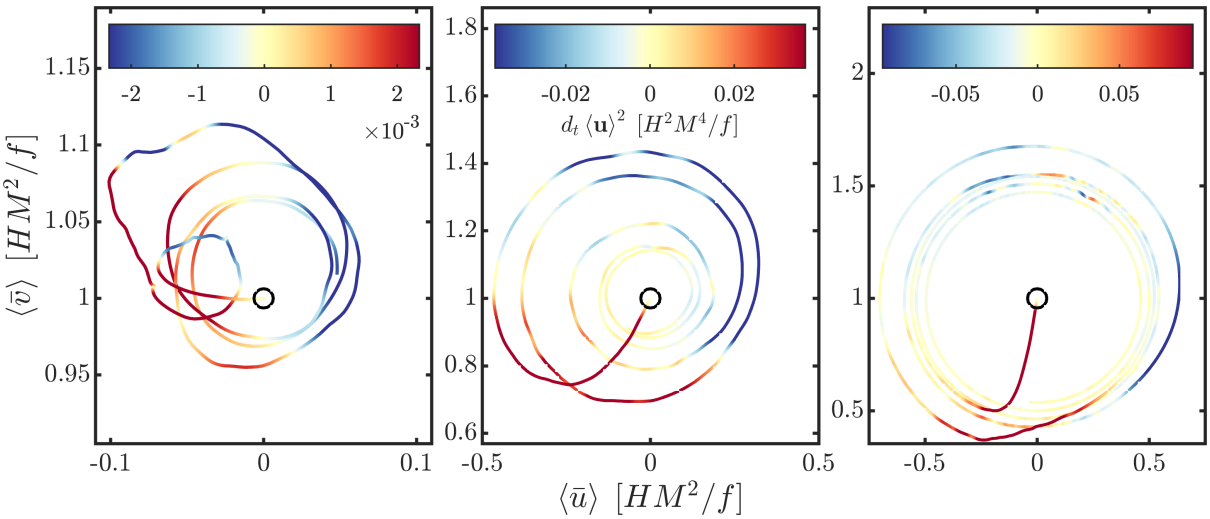

Figure 20: Hodographs in the mean total u and v phase space for each of the 2D simulations plotted for the first 5 inertial periods, shown for increasing front strength from left to right. The trajectories are coloured with the time-rate of change of the mean flow speed, and correspond closely with the ageostrophic shear production. The angle of the initial departure indicates how extreme the geostrophic adjustment is. For relatively weak fronts, the front remains nearly in geostrophic balance while an across-front flow slumps the front over. This lies in stark contrast to strong fronts where the thermal wind shear is more well-mixed before the front can react.

accessed by ageostrophic shear production ($\mathcal{P}_a$ in equation (32)), which energises the inertial oscillation by completing the mixing of the thermal wind shear. While it is not shown in the energy transfers on the top panel of figure 21, the conversion of MPE into MKE and back again comprises the inertial oscillations. This exchange is via the mean advection of the horizontal buoyancy gradient,

$$\Gamma^{-1} \langle \bar{u}\, z \rangle \,, \tag{43}$$

and from which energy can only be extracted from this oscillation via the ageostrophic shear production.

4.1.3 Scaling Arguments

By scaling the TKE budget components by the geostrophic KE, we might expect the geostrophic shear production, and therefore the magnitude of the TKE itself to collapse. While this may initially be the case, many of the differences in the later evolution must be understood in the context of other energetics quantity scalings.

This scaling exceptionally doesn't collapse for $\Gamma = 1$, where the buoyancy production also contributes to the TKE budget (figure 22). This PE is accessed only by the non-monotonic mean shear, $\bar{u}(z)$, which can generate gravitationally-unstable regions near the boundaries by differentially advecting the horizontal buoyancy gradient vertically over itself, where it can then be converted to TKE.

For stronger fronts, the transient and "bursty" turbulence appears to limit the amount of dissipation and results in more persistent and coherent inertial oscillations. The turbulence dissipation time-scale, $\tau_d f \sim \Gamma^{-1}$, being much shorter than an inertial period, seems to explain these transient dynamics observed in strong fronts during destratification, and which are separated by periods of nearly laminar inertial oscillations. This means that for $\Gamma \gtrsim 100$, the relevant time-scale setting the mean rate of energy removal from the system becomes the inertial time, $\tau_d f \sim 1$, which is consistent with the decrease in total dissipated energy for $\Gamma = 100$ in figure 22.

4.2 Late-Time Dynamics

The background inertial oscillations of the front even at late times can excite a number of different dynamics based on their amplitude (and consequently the strength of the front). In weak fronts and small inertial oscillations, multiple frontlets form and continuous weak turbulence is supported until equilibration. Fronts of intermediate strength are seen to undergo tertiary SI, driving larger-scale modes, which upon stabilisation remain as fossil subinertial oscillations. Finally, strong fronts generating large

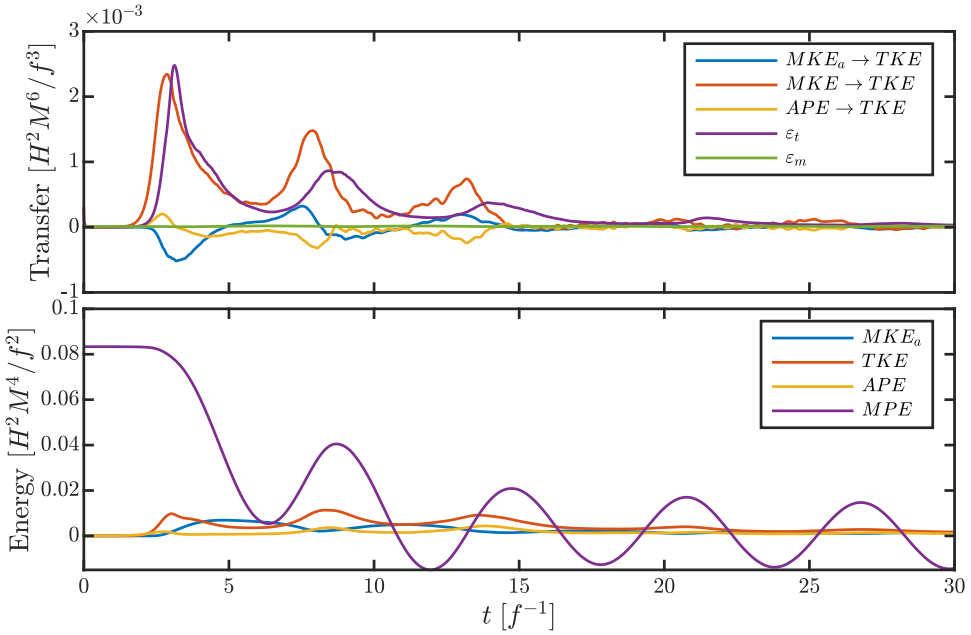

Figure 21: Summary of the ageostrophic energy transfers and evolution in the $\Gamma = 10$ simulation. The initial transfer of energy from MKE into TKE and onto ageostrophic MKE is later countered as the mean ageostrophic energy is released back into TKE when the inertial oscillations themselves are shear unstable.

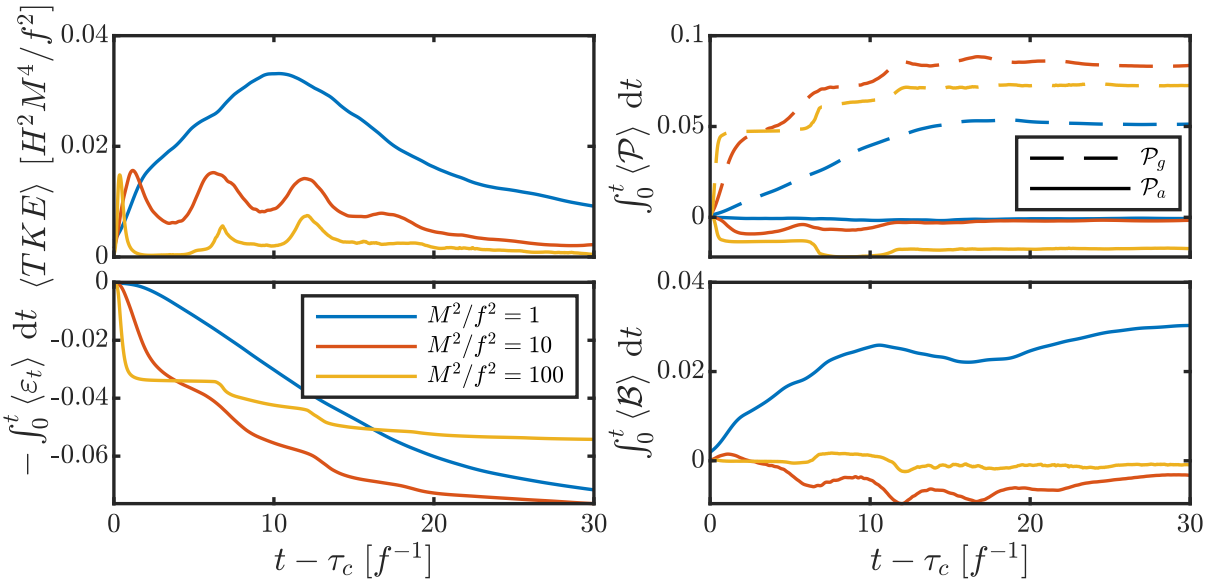

Figure 22: Comparison of the evolution of the TKE budget components for various front strengths.

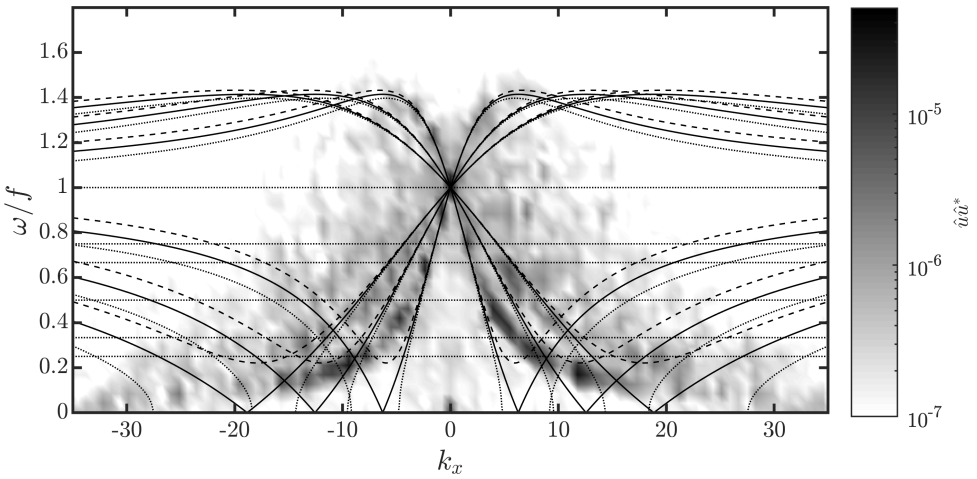

Figure 23: Wavenumber-frequency diagram for $\Gamma = 1$. The linear dispersion relation is shown for each $Ri = 0.9$ (dotted), 1 (solid), and 1.1 (dashed). Three groupings set the scale of k_x (from inside out): $\lambda_z = 1$, 1/2, and 1/3.

inertial oscillations exhibit "bursty" behaviour due to the catastrophic roll-up of these tertiary SI modes during periods of destratification, and which are followed by nearly laminar phases of the oscillation. In each case, turbulence remnant from adjustment or from these secondary dynamics injects positive PV fluid (by enhancing fluxes) from the boundaries, and ultimately results in stabilisation of SI on remarkably similar timescales.

4.2.1 Subinertial Oscillations

Following breakdown of the primary SI modes to turbulence, Griffiths (2003) (in the atmosphere) and Taylor and Ferrari (2009) (in the ocean mixed layer) both found that if the new state was still unstable, an SI mode with a longer wavelength (~ 10 times larger) began to grow, consistent with using an effective turbulent viscosity much larger than the molecular viscosity. This larger-scale SI mode, selected by self-organised criticality towards a wavelength which is balanced against KHI, may then persist for long times (on top of the laminarised inertial shear oscillations) as a fossil remnant. These oscillations nearly paralleling the slumped isopycnal lines are seen at late times in the bottom row of figure 15.

These tertiary SI modes as described in section 3.2.3 are also responsible for the bursty behaviour found in Thomas et al. (2016), if their growth rate is sufficiently fast compared to the inertial period, so that they break down (either partially, or catastrophically) via KHI during periods of minimum stratification. This is found to occur for stronger fronts, with $\Gamma \gtrsim 100$, as seen in the bottom right panel of figure 15. During these explosive growth periods, $\mathcal{P}_g > 0$ and $\mathcal{P}_a < 0$, indicating that the energy pathway connects from the geostrophic flow, into SI, and then energising the secondary circulations and inertial oscillation. This is indeed what is observed in the right hodograph of figure 20, where the amplitude of the inertial oscillation further increases in the second two periods.

In the less extreme case (for smaller Γ) when the tertiary SI growth rate is too slow to eventually break down by KHI before PV becomes positive, then the remnant SI mode APE may generate subinertial or "slantwise inertial" oscillations (c.f. section 2.1.3). This potential conversion from SI to subinertial gravity mode as Ri_g becomes greater than 1 is apparent from equation (2.1.3), where $\omega_{\min}$ just becomes real valued. These subinertial modes can oscillate at frequencies $f_{\text{eff}} < \omega < N$, where this $f_{\text{eff}} < f$, and appear along with their harmonics in figure 23.

These subinertial oscillations are also observed to undergo critical reflection on the horizontal boundaries for $\Gamma = 10$ and 100. This is because an inertial wave travelling vertically within a front (i.e. with $\omega = f_{\text{eff}}$), upon reflecting off of the horizontal boundaries only has the exactly horizontal ray path available. This horizontal ray has 0 group speed, and so energy is concentrated near the point of reflection, eventually breaking down into turbulence. Grisouard and Thomas (2015) showed that these critically-reflecting impingement points can result in gravity bores, which Pham and Sarkar (2018) have also found in all of the finite fronts they considered. This gravity bore not only dissipates wave energy, but also enhances the transfer of potential energy (in the horizontal gradient) into TKE and thus towards dissi-

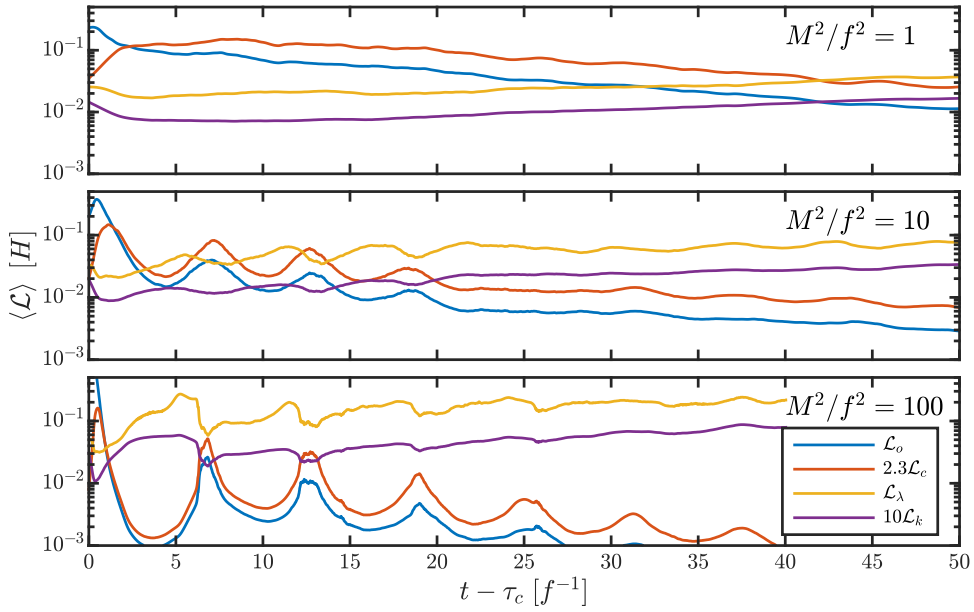

Figure 24: Evolution of the characteristic turbulent length-scales: The Ozmidov buoyancy scale, the Corrsin shear scale, the Taylor turbulence microscale, and the Kolmogorov length-scale. At late times in the $\Gamma = 1$ simulation, and throughout the $\Gamma = 100$ simulation, the Ozmidov scale is smaller than the smallest turbulent eddies, implying that the energy pathway into BPE via overturning isopycnals is cutoff. This 'buoyant-inertial-viscous transition' occurs later for weak fronts.

pation. Critical reflection thus may be a crucial mechanism for damping the large-scale inertial motions, particularly in strong fronts.

4.2.2 Energy Pathways

Whereas the characteristics of SI and the turbulent transition sets the amplitude of the inertial shear oscillations, the late-time evolution of the ageostrophic circulations are dictated by the intensity of the turbulence relative to how quickly the front has restratified. The evolution of the characteristic turbulence length-scales, notably the Ozmidov length and the Taylor microscale, are one such metric to give insight into the pathways for energy following destabilisation and how this varies based on the strength of the front.

The Ozmidov length-scale,

$$\mathcal{L}_o = \sqrt{\frac{\langle \varepsilon \rangle}{\langle N^3 \rangle}} \tag{44}$$

is a measure for the scale of the largest possible isopycnal overturns. Similarly, the Taylor microscale,

$$\mathcal{L}_\lambda = \sqrt{\frac{5\nu \langle u_i^2 \rangle}{\langle \varepsilon \rangle}} \tag{45}$$

is the characteristic length of the small-scale turbulent eddies. Comparing these length-scales in figure 24, we see that in weak fronts, $\mathcal{L}_\lambda \ll \mathcal{L}_o$, indicating that a large majority of the turbulent energy is able to stir, and eventually mix the background buoyancy, thus raising the PE. This is compared to the $\Gamma = 100$ front, where frequently $\mathcal{L}_\lambda > \mathcal{L}_o$, and so the eddies are too large to overturn the vertical stratification. However, these large eddies — larger than the Corrsin (shear) scale,

$$\mathcal{L}_c = \sqrt{\frac{\langle \varepsilon \rangle}{\langle S^3 \rangle}} \tag{46}$$

— are preferentially sheared by the background velocity. The tilting of these modes contributes to shear production of MKE, implying an alternative energy pathway into the ageostrophic MKE following Buoyant-Inertial-Viscous Transition.

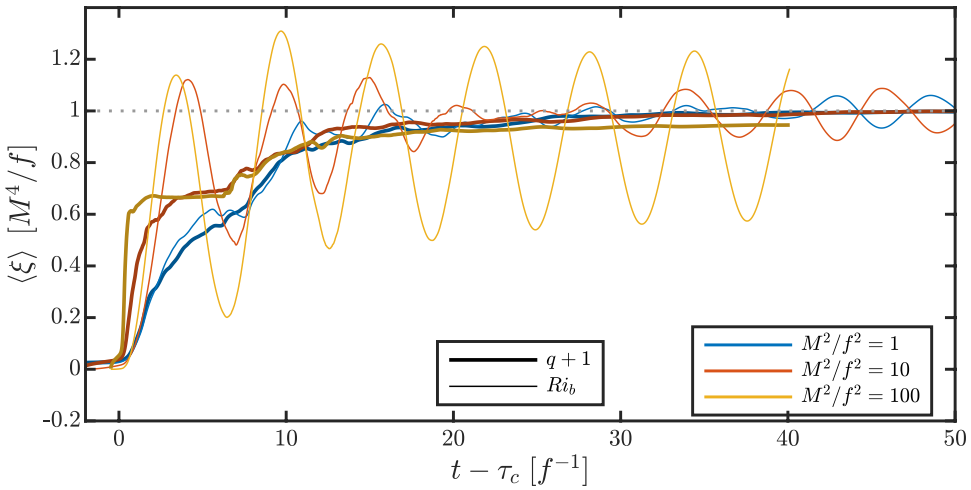

Figure 25: The evolution of the domain-integrated PV and balanced Richardson number, showing the connection of the PV flux rate into the domain in relaxing the mean stratification.

4.2.3 Damping to Equilibrium

The path towards equilibration is ultimately constrained by PV (Rotunno and Thorpe, 1989). SI unstable regions are only stabilised by boundary fluxes and turbulent mixing transporting PV. These turbulent fluxes relax the PV towards 0 over time and take the front to its restratified equilibrium. Considering the potential vorticity in our closed domain expressed in geostrophic units,

$$q = \Gamma^{-1} \left(f^2/M^4 \partial_z \bar{b} - 1 - \partial_z \bar{v}_a \right), \tag{47}$$

makes clear how the restratification ($\partial_z \bar{b}$) is compensated for during inertial oscillations by the baroclinic PV term due to the ageostrophic across-front vorticity. This suggests two natural diagnostics: First, the difference between these two terms compensating each other, $\Gamma q + 1$, is just a rescaled PV, but nonetheless is a good measure for the equilibration progress. This can be directly compared to the balanced Richardson number, $Ri_b \equiv f^2/M^4 \partial_z \bar{b}$, a metric for the inertial oscillations. These two quantities are shown evolving in figure 25 for each of the three simulations. When the front is balanced, $q+1$ and Ri_b lie on top of each other, as they do initially. Likewise, at very late times when the inertial oscillations apparent in Ri_b would have decayed these two lines would again coincide. The quasi-balanced evolution for the weakest ($\Gamma = 1$) front as pointed out in 4.1.1 is also apparent looking at this metrics, because throughout the equilibration $q+1$ and Ri_b never differ by much.

Going beyond this diagnostic, we can understand the mechanisms for PV increase by horizontally-averaging the PV equation (10),

$$\frac{\partial \langle q \rangle}{\partial t} = -\frac{\partial}{\partial z} \left\langle qw - \frac{1}{RePr} \nabla^2 b (\omega_z + f) + \frac{1}{Re} \left(\nabla b \times \nabla^2 \mathbf{u} \right) \cdot \hat{\mathbf{k}} \right\rangle. \tag{48}$$

The domain-integrated PV can thus be restored to 0 by three mechanisms:

- Boundary fluxes of buoyancy and momentum
- Viscous generation of vorticity at the boundaries
- Lateral fluxes of positive PV from nearby stable regions

However, in our closed domain the only surface fluxes of PV are due to a non-zero $\nabla^2 b$ and $\nabla^2 v$ at the boundaries. Turbulence increases the curvature of these fields and thus can enhance the flux of PV into the domain. Consequently, the largest PV fluxes are associated with the most turbulent periods during destratification.

It therefore would make sense that the rate of PV flux scales directly with strength of the front, as apparent for early times in figure 25. However, similar to the dissipation scaling in section 4.1.3, while the instantaneous flux may increase with Γ, the relatively quiescent oscillation phases in the strong fronts mean that the time-averaged PV flux is nearly independent of front strength. This may also be related to the self-regulating feedback between the enhanced turbulent mixing energised by SI, which itself (by driving PV positive) stabilises SI. The resulting nearly Γ-invariant decay rate towards $q = 0$ seen in figure 25 has a uniform damping time-scale of $\tau_q f \approx 5.5$, despite the first inertial period drastically differing.

5 Conclusions

Frontal systems in the upper ocean are quite common — from the strong persistent western boundary currents, down to transient strain-generated frontal features in the open ocean. While these fronts have a broad range in the strength of the horizontal stratification, M^2/f^2, we have found that there are dynamical similarities in the evolutionary phases across these fronts. Still, many of the secondary dynamics excited and the details of adjustment greatly depend on the strength of the front. We have understood these differences in the context of the mechanism often responsible for destabilising the front: symmetric instability. Symmetric instability was found to set the geostrophic shear mixing fraction and thus the amplitude of large-scale inertial oscillations of the front, extending the results of Tandon and Garrett (1994) to account for viscosity and mixing over a finite time interval. The presented analysis supported by numerical simulations, explains the quasi-balanced adjustment towards equilibration in weak fronts, in contrast to the drastic geostrophic adjustment when strong fronts become unbalanced.

Finite fronts have been all but mostly neglected in the literature, but their differences in equilibration due to *horizontal* fluxes may be important for understanding and eventually modelling their impact on the larger scales in the ocean. In particular, it is known that a purely geostrophic adjustment generates a frontal discontinuity for $Ro > 1$ (Blumen, 2000), but as we have already observed in a number of scoping runs, the conditions and process of generating a bore-like boundary gravity current are yet to be understood. Still many of these generic processes in fronts are now much more well understood following this study of horizontally-infinite fronts. However, the relevance of this approximation is limited, particularly for $\Gamma \gtrsim 100$, as strong fronts tend to also be relatively sharp (i.e. narrow). Lateral mixing, spreading, and fluxes of PV are unique processes to finite fronts, and depend strongly on the profile and width. The varying thermal wind shear across the front (generating ω_z) also means that the inertial frequency varies, which can modify the properties of symmetric instability. These details of symmetric instability in fronts with finite support, as well as the potential now to develop inertial instability will be the subject of a follow-up publication.

References

S. D. Bachman, B. Fox-Kemper, J. R. Taylor, and L. N. Thomas. Parameterization of Frontal Symmetric Instabilities. I: Theory for Resolved Fronts. *Ocean Modelling*, 109:72–95, Jan. 2017.

R. Barkan, K. B. Winters, and S. G. Llewellyn Smith. Energy Cascades and Loss of Balance in a Reentrant Channel Forced by Wind Stress and Buoyancy Fluxes. *Journal of Physical Oceanography*, 45(1):272–293, Jan. 2015.

W. Blumen. Inertial Oscillations and Frontogenesis in a Zero Potential Vorticity Model. *Journal of Physical Oceanography*, 30(1):31–39, 2000.

L. Brannigan, D. P. Marshall, A. C. N. Garabato, A. J. G. Nurser, J. Kaiser, L. Brannigan, D. P. Marshall, A. C. N. Garabato, A. J. G. Nurser, and J. Kaiser. Submesoscale Instabilities in Mesoscale Eddies. *Journal of Physical Oceanography*, 47(12):3061–3085, Dec. 2017.

X. Capet, J. C. McWilliams, M. J. Molemaker, and A. F. Shchepetkin. Mesoscale to Submesoscale Transition in the California Current System. Part I: Flow Structure, Eddy Flux, and Observational Tests. *Journal of Physical Oceanography*, 38(1):29–, 2008.

J. Charney. Geostrophic turbulence. *Journal of the Atmospheric Sciences*, 28:1088, 1971.

J. G. Charney. The Dynamics of Long Waves in a Baroclinic Westerly Current. *Journal of Atmospheric Sciences*, 4(5):136–162, Oct. 1947.

E. D'Asaro, C. Lee, L. Rainville, R. Harcourt, and L. Thomas. Enhanced Turbulence and Energy Dissipation at Ocean Fronts. *Science*, 332(6):318–, Apr. 2011.

E. T. Eady. Long Waves and Cyclone Waves. *Tellus*, 1(3):33–52, Dec. 1949.

B. Fox-Kemper, R. Ferrari, and R. Hallberg. Parameterization of Mixed Layer Eddies. Part I: Theory and Diagnosis. *Journal of Physical Oceanography*, 38(6):1145–, 2008.

S. D. Griffiths. Nonlinear vertical scale selection in equatorial inertial instability. *Journal of the Atmospheric Sciences*, 2003.

N. Grisouard and L. N. Thomas. Critical and near-critical reflections of near-inertial waves off the sea surface at ocean fronts. *Journal of Fluid Mechanics*, 765:273–302, Jan. 2015.

T. W. N. Haine and J. Marshall. Gravitational, Symmetric, and Baroclinic Instability of the Ocean Mixed Layer. *Journal of Physical Oceanography*, 28(4):634–658, 1998.

P. H. Haynes and M. E. McIntyre. On the Conservation and Impermeability Theorems for Potential Vorticity. *Journal of the Atmospheric Sciences*, 47(16):2021–2031, 1990.

B. J. Hoskins. The role of potential vorticity in symmetric stability and instability. *Quarterly Journal of the Royal Meteorological Society*, 100(425):480–482, July 1974.

B. J. Hoskins and F. P. Bretherton. Atmospheric Frontogenesis Models: Mathematical Formulation and Solution. *Journal of Atmospheric Sciences*, 29(1):11–37, Jan. 1972.

B. L. Hua, D. W. Moore, and S. L. Gentil. Inertial nonlinear equilibration of equatorial flows. *Journal of Fluid Mechanics*, 331:345–371, Jan. 1997.

S. Jinadasa, I. Lozovatsky, Planella-Morató, J. Nash, J. MacKinnon, A. Lucas, H. Wijesekera, and H. Fernando. Ocean turbulence and mixing around Sri Lanka and in adjacent waters of the northern Bay of Bengal. *Oceanography*, 29, 2016.

T. M. Joyce, L. N. Thomas, and F. Bahr. Wintertime observations of Subtropical Mode Water formation within the Gulf Stream. *Geophysical Research Letters*, 36(2), Jan. 2009.

H.-L. Kuo. Symmetrical Disturbances In A Thin Layer Of Fluid Subject To A Horizontal Temperature Gradient And Rotation. *Journal of Meteorology*, 11(5):399–411, Oct. 1954.

R. Legeckis. Long Waves in the Eastern Equatorial Pacific Ocean: A View from a Geostationary Satellite. *Science*, 197(4):1179–1181, Sept. 1977.

J. Marshall, A. Andersson, N. Bates, W. Dewar, S. Doney, J. Edson, R. Ferrari, G. Forget, D. Fratantoni, M. Gregg, T. Joyce, K. Kelly, S. Lozier, R. Lumpkin, G. Maze, J. Palter, R. Samelson, K. Silverthorne, E. Skyllingstad, F. Straneo, L. Talley, L. Thomas, J. Toole, and R. Weller. The Climode Field Campaign: Observing the Cycle of Convection and Restratification over the Gulf Stream. *Bulletin of the American Meteorological Society*, 90(9):1337–, 2009.

J. C. McWilliams, M. J. Molemaker, and I. Yavneh. From Stirring to Mixing of Momentum: Cascades from Balanced Flows to Dissipation in the Oceanic Interior. *Proceedings Hawaiian Winter Workshop*, Jan. 2001.

M. J. Molemaker, J. C. McWilliams, and X. Capet. Balanced and unbalanced routes to dissipation in an equilibrated Eady flow. *Journal of Fluid Mechanics*, 654:35–63, June 2010.

H. T. Pham and S. Sarkar. Ageostrophic Secondary Circulation at a Submesoscale Front and the Formation of Gravity Currents. *Journal of Physical Oceanography*, 48(10):2507–2529, Oct. 2018.

S. Ren. Normal modes in the symmetric stability problem in a vertically bounded domain. *Geophysical & Astrophysical Fluid Dynamics*, 102(4):333–348, Aug. 2008.

P. B. Rhines. Mixing and Large-Scale Ocean Dynamics. In *Small-Scale Turbulence and Mixing in the Ocean - Proceedings of the 19th International Liege Colloquium on Ocean Hydrodynamics*, pages 263–284. Elsevier, 1988.

R. Rotunno and A. J. Thorpe. Nonlinear Aspects of Symmetric Instability. *Journal of the Atmospheric Sciences*, 46(9):1285–1299, May 1989.

I. Savelyev, L. N. Thomas, G. B. Smith, Q. Wang, R. K. Shearman, T. Haack, A. J. Christman, B. Blomquist, M. Sletten, W. D. Miller, and H. J. S. Fernando. Aerial Observations of Symmetric Instability at the North Wall of the Gulf Stream. *Geophysical Research Letters*, 45(1):236–244, Jan. 2018.

M. Solberg. Le mouvement d'inertie de l'atmosphere stable et son role dans le theorie des cyclones. *Union Geodesique et Geophisique internationale VIeme assemblee*, pages 66–82, 1936.

M. A. Stamper and J. R. Taylor. The transition from symmetric to baroclinic instability in the Eady model. *Ocean Dynamics*, 67(1):1–16, Nov. 2016.

P. H. Stone. On Non-Geostrophic Baroclinic Stability. *Journal of the Atmospheric Sciences*, 23(4): 390–400, 1966.

P. H. Stone. On Non-Geostrophic Baroclinic Stability: Part II. *Journal of the Atmospheric Sciences*, 27 (5):721–726, Aug. 1970.

P. H. Stone. Baroclinic stability under non-hydrostatic conditions. *Journal of Fluid Mechanics*, 45(04): 659, 1971.

A. Tandon and C. Garrett. Mixed Layer Restratification Due to a Horizontal Density Gradient. *Journal of Physical Oceanography*, 24(6):1419–, 1994.

J. R. Taylor. *Numerical Simulations of the Stratified Oceanic Bottom Boundary Layer*. PhD thesis, University of California, San Diego, 2008.

J. R. Taylor and R. Ferrari. On the equilibration of a symmetrically unstable front via a secondary shear instability. *Journal of Fluid Mechanics*, 622:103–11, Feb. 2009.

J. R. Taylor and R. Ferrari. Buoyancy and Wind-Driven Convection at Mixed Layer Density Fronts. *Journal of Physical Oceanography*, 40(6):1222–1242, June 2010.

L. N. Thomas and C. M. Lee. Intensification of Ocean Fronts by Down-Front Winds. *Journal of Physical Oceanography*, 35(6):1086–1102, June 2005.

L. N. Thomas and J. R. Taylor. Reduction of the usable wind-work on the general circulation by forced symmetric instability. *Geophysical Research Letters*, 37(18), Sept. 2010.

L. N. Thomas and J. R. Taylor. Damping of inertial motions by parametric subharmonic instability in baroclinic currents. *Journal of Fluid Mechanics*, 743:280–294, Mar. 2014.

L. N. Thomas, J. R. Taylor, R. Ferrari, and T. M. Joyce. Symmetric instability in the Gulf Stream. *Deep-Sea Research Part II*, 91(C):96–110, July 2013.

L. N. Thomas, J. R. Taylor, E. A. D'Asaro, C. M. Lee, J. M. Klymak, and A. Shcherbina. Symmetric Instability, Inertial Oscillations, and Turbulence at the Gulf Stream Front. *Journal of Physical Oceanography*, 46(1):197–217, Jan. 2016.

A. F. Thompson, A. Lazar, C. Buckingham, A. C. Naveira Garabato, G. M. Damerell, and K. J. Heywood. Open-Ocean Submesoscale Motions: A Full Seasonal Cycle of Mixed Layer Instabilities from Gliders. *Journal of Physical Oceanography*, 46(4):1285–1307, Apr. 2016.

G. K. Vallis. *Atmospheric and Oceanic Fluid Dynamics*. Fundamentals and Large-scale Circulation. Cambridge University Press, Nov. 2006.

S. J. Warner, R. M. Holmes, E. H. M Hawkins, M. S Hoecker-Martínez, A. C. Savage, and J. N. Moum. Buoyant Gravity Currents Released from Tropical Instability Waves. *Journal of Physical Oceanography*, 48(2):361–382, Feb. 2018.

J. E. Weber. Symmetric instability of stratified geostrophic flow. *Tellus*, 32(2):176–185, 1980.

D. B. Whitt and L. N. Thomas. Near-Inertial Waves in Strongly Baroclinic Currents. *Journal of Physical Oceanography*, 43(4):706–725, Apr. 2013.